NAVAL POSTGRADUATE SCHOOL
MONTEREY, CALIFORNIA

THESIS

A CASE STUDY OF DIURNAL VARIATION OF CONVECTION AND MESOSCALE MODELING DURING TOGA-COARE

by

Patrick L. Waring

December, 1994

Thesis Advisor: Teddy R. Holt

REPORT DOCUMENTATION PAGE

Form Approved OMB No. 0704-0188

1. AGENCY USE ONLY *(Leave blank)*

2. REPORT DATE December 1994

3. REPORT TYPE AND DATES COVERED Master's Thesis

4. TITLE AND SUBTITLE A CASE STUDY OF DIURNAL VARIATION OF CONVECTION AND MESOSCALE MODELING DURING TOGA-COARE

5. FUNDING NUMBERS

6. AUTHOR(S) Patrick L. Waring

7. PERFORMING ORGANIZATION NAME(S) AND ADDRESS(ES)
Naval Postgraduate School
Monterey CA 93943-5000

8. PERFORMING ORGANIZATION REPORT NUMBER

9. SPONSORING/MONITORING AGENCY NAME(S) AND ADDRESS(ES)

10. SPONSORING/MONITORING AGENCY REPORT NUMBER

11. SUPPLEMENTARY NOTES The views expressed in this thesis are those of the author and do not reflect the official policy or position of the Department of Defense or the U.S. Government.

12a. DISTRIBUTION/AVAILABILITY STATEMENT
Approved for public release; distribution is unlimited.

12b. DISTRIBUTION CODE

13. ABSTRACT *(maximum 200 words)*

Infrared satellite images from the TOGA-COARE domain have been objectively processed to reveal the distribution of cloud clusters with temperatures of a given threshold for two 48-h periods (14-15 January and 18-19 January 1993). Cold cloudiness is examined with a threshold of less than 208°K and moderately cold cloudiness is examined with a threshold of less than 235°K. Cloud cluster sizes are found to have a log-normal distribution. Cluster size ranges for the given temperature thresholds are found to be smaller for 14-15 January than for 18-19 January, and smaller overall than previous climatological studies. Due to synoptic-scale variability, the diurnal cycle is more apparent during 18-19 January with deep convection peaking before dawn, and then moderately cold cloud area expanding in the afternoon. Smaller clusters have a smaller diurnal signal than larger clusters. The NPS/NRL mesoscale model demonstrates skill in the forecast of total cloud cover with a model integration of up to 24 hours. The model is found to over-forecast cloud cluster size and to show minimal skill in depicting a diurnal signal in convection.

14. SUBJECT TERMS Diurnal Convection, Mesoscale Modeling.

15. NUMBER OF PAGES 94

16. PRICE CODE

17. SECURITY CLASSIFICATION OF REPORT Unclassified

18. SECURITY CLASSIFICATION OF THIS PAGE Unclassified

19. SECURITY CLASSIFICATION OF ABSTRACT Unclassified

20. LIMITATION OF ABSTRACT UL

NSN 7540-01-280-5500

Standard Form 298 (Rev. 2-89)
Prescribed by ANSI Std. 239-18 298-102

A CASE STUDY OF DIURNAL VARIATION OF CONVECTION AND MESOSCALE MODELING DURING TOGA-COARE

by
Patrick L. Waring
Lieutenant, United States Navy
B.S., University of Nebraska, 1985

Submitted in partial fulfillment
of the requirements for the degree of

MASTER OF SCIENCE IN METEOROLOGY AND PHYSICAL OCEANOGRAPHY

from the

NAVAL POSTGRADUATE SCHOOL
December 1994

Author: ______________________
Patrick L. Waring

Approved by: Teddy R. Holt
Teddy R. Holt, Thesis Advisor

Russell L Elsberry
Russell L. Elsberry, Second Reader

RLHaney
Robert L. Haney, Chairman
Department of Meteorology

ABSTRACT

Infrared satellite images from the TOGA-COARE domain have been objectively processed to reveal the distribution of cloud clusters with temperatures of a given threshold for two 48-h periods (14-15 January and 18-19 January 1993). Cold cloudiness is examined with a threshold of less than 208°K and moderately cold cloudiness is examined with a threshold of less than 235°K. Cloud cluster sizes are found to have a log-normal distribution. Cluster size ranges for the given temperature thresholds are found to be smaller for 14-15 January than for 18-19 January, and smaller overall than previous climatological studies. Due to synoptic-scale variability, the diurnal cycle is more apparent during 18-19 January with deep convection peaking before dawn, and then moderately cold cloud area expanding in the afternoon. Smaller clusters have a smaller diurnal signal than larger clusters. The NPS/NRL mesoscale model demonstrates skill in the forecast of total cloud cover with a model integration of up to 24 hours. The model is found to over-forecast cloud cluster size and to show minimal skill in depicting a diurnal signal in convection.

TABLE OF CONTENTS

ACKNOWLEDGMENT

The author would like to thank Dr. Teddy Holt for his guidance and support in the completion of this thesis. His patience, knowledge and enthusiasm kept me going till the end. I would also like to thank Professor Russell Elsberry. His knowledge allowed me to maintain the focus of my topic.

Most importantly, I would like to thank my wife, Sharon, for her patience and understanding, without which the completion of this thesis would not have been possible. And finally, I dedicate this thesis to our son Benjamin, who was born during my time at the Naval Postgraduate School. He continues to remind me of the important things in life.

I. INTRODUCTION

Satellite infrared (IR) imagery is a highly detailed data source, both temporally and spatially, for examining diurnal variations in convection. Tropical deep convective clouds are especially easy to distinguish in IR imagery because of the large temperature contrast between the cold cloud tops and the warm surface in the tropics. However, the interpretation of that data is extremely complex in that we have to deal with a temperature range through the depth of the atmosphere, as well as a time evolution in cloud temperatures. Also, the clouds are organized into clusters that are constantly changing in areal extent due not only to diurnal influences, but also from synoptic variations.

Previous studies such as Gray and Jacobson (1977), Albright et al. (1985), and Mapes and Houze (1993) have examined the diurnal variation in tropical areas. However, they have all looked at the diurnal variation as a larger scale phenomena. This analysis consists of a case study in which the diurnal signal in cloudiness during the Tropical Ocean-Global Atmosphere (TOGA) Coupled Ocean-Atmosphere Response Experiment (COARE) in the tropical western Pacific warm pool region is diagnosed. The specific focus is on the mesoscale convection in the domain of the Intensive Flux Array (IFA) shown in Fig. 1.

The second objective is to compare output from a mesoscale numerical model with the analysis of the satellite data. Soundings during the Intensive Observation Phase (IOP) of TOGA-COARE will also be used to evaluate the realism of the structures predicted by the model.

II. TOGA-COARE

The TOGA program is a component of the World Climate Research Programme (WCRP 1985) aimed at the prediction of climate phenomena. TOGA focuses on the tropical oceans and their relationship to the global atmosphere (Webster and Lukas 1992). TOGA-COARE was undertaken to gain a better understanding of the air-ocean environment of the tropical warm-pool region of the western Pacific Ocean. TOGA-COARE included a number of Intensive Observation Phases (IOP) between 1 November 1992 and 28 February 1993.

TOGA-COARE was located in the western Pacific warm-pool region between 20°N and 20°S that is bounded by Indonesia on the west and the dateline on the east. As illustrated in Fig. 1, COARE included a Large-Scale Array (LSA) bounded by 10°N to 10°S and 140°E to 180°E. This region was chosen because it contains the warmest water, is the most convectively disturbed, and receives the greatest amount of precipitation in the tropical Pacific Ocean (Webster and Lukas 1992). The innermost domain is the Intensive Flux Array (IFA). The IFA is in a polygon formed by the islands of Kapingamarangi (KAP) and Kavieng (KAV), and by the ships R/V Shiyan 3 (XP3) and R/V Kexue 1 (SC1) located near 2°S, 158°E and 4°S, 155°E respectively. Other key locations include the islands of Manus (MAN) and Nauru (NAU).

Fig. 1 also illustrates the inner-most grid of the Naval Postgraduate School/Naval Research Laboratory (NPS/NRL) triply nested mesoscale model, which will be described in Chapter IV. The LSA and the model inner grid also correspond to the two domains of Geostationary Meteorological Satellite (GMS) imagery used in this study. It should be noted that the term IFA may be used when discussing the inner grid of the model as well as the inner-most observational array.

A. PURPOSE

One of the scientific objectives of TOGA-COARE is to determine the magnitude (and significance for longer-term models) of short time-scale variability in the fluxes of heat, moisture, and momentum--hourly, diurnal, and episodal (Webster and Lukas 1992). The primary purpose of this analysis is to conduct a case study examining the diurnal nature of convection in the TOGA-COARE domain through the analysis of infrared satellite imagery. A second purpose is to compare the satellite analysis with output from a mesoscale numerical model to determine how realistically the model portrays cloud features and any diurnal signal that is present.

B. DATA

Data used in this study include the following:

- Geostationary Meteorological Satellite (GMS) infrared imagery. The infrared radiometer on the satellite receives energy from 10.5-12.5 μm and has a resolution at the subsatellite point of 5.0 km. The TOGA imagery was captured and archived on CD-ROM by the University of Hawaii-Manoa (Flament and Bernstein 1993). The imagery was downloaded as PostScript files from the CD-ROM, converted into binary format, and then displayed. The byte values from the imagery were converted to temperature values via a linear conversion (Flament and Bernstein 1993).

- Soundings during the IOPs of TOGA-COARE. Only soundings from the six sites in Fig. 1 were used in this study. The sounding data were interpolated to 10 seconds from the original 2 second raw thermodynamic data. Due to pre-flight environmental effects on the sonde sensor arm, in some cases the temperature and humidity data were corrected in the lowest levels.

- Fields predicted by the NPS/NRL triply nested mesoscale model.

Other data and sensors utilized during TOGA-COARE (but not used in this study) include buoy observations, surface weather observations, ground-based radar and other remote sensors including satellite microwave and aircraft radar.

III. CLIMATOLOGY

A. TOGA CLIMATOLOGY

A climatological analysis of the TOGA-COARE domain was prepared by Schrage and Vincent (1993) based on data from January 1985 through December 1990. Their climatology emphasizes the period from November through February, which corresponds to the Intensive Observing Period (IOP) of TOGA-COARE during 1993. A brief overview of Schrage and Vincent's (1993) study is given here to provide a large-scale framework for this satellite and modeling study.

1. Pressure/Height Patterns

The climatological mean sea-level pressure (MSLP) distribution for January is given in Fig. 2. The prominent feature is the equatorial trough stretching ENE from northern Australia into the central Pacific. This trough lies to the south of the LSA. Notice that the TOGA-COARE area, as well as the tropics in general, is characterized by a very flat MSLP signature.

The monthly mean geopotential height analyses for January at 500 and 200 hPa are given in Figs. 3 and 4. At 500 hPa, ridges of higher heights extend across tropical/subtropical latitudes of both hemispheres. At 200 hPa, a broad near-equatorial ridge extends across the western Pacific as a permanent feature of the upper-tropospheric circulation during the northern winter months. This ridge is located along the northern border of the LSA. There is also an elongated ridge in the Southern Hemisphere that stretches eastward from northern Australia to the central Pacific and then southeast toward higher (southern) latitudes.

2. Streamlines and Isotachs

Streamline and isotach patterns for the surface, 850, and 200 hPa are presented in Fig. 5. Whereas the 200 hPa (Fig. 5a) flow west of about 170°W is from the Southern (summer)

Hemisphere to the Northern (winter) Hemisphere, the meridional flow is reversed at the surface. An axis of cyclonic flow exists at the surface (anticyclonic at 200 hPa) between 10°S to 20°S and from about 130°E to 180°E. This suggests that the ascent branch of the Hadley circulation cell is dominating the flow pattern of the area. A pair of 200 hPa anticyclones straddle the equator near 160°E. The isotach analysis at 200 hPa (Fig. 5d) has a band of easterlies stretching across the equator from 100°E to 150°E. At 850 hPa (Fig. 5f), the axis of maximum easterlies extends westward from 0°N, 130°W to 10°N, 170°E and then to 10°N, 110°E. At the surface, the strongest winds are the northeast trades that stretch across the Pacific along 10°N.

3. Divergence

At 200 hPa (Fig. 6a), a band of maximum divergence located over Indonesia extends eastward and southeastward toward the central South Pacific. This segment corresponds to the upper-level outflow associated with the South Pacific Convergence Zone (SPCZ). A secondary axis of much weaker and less continuous divergence extends along 5-10°N across the Pacific, which corresponds with the location of the Inter-Tropical Convergence Zone (ITCZ). At 850 hPa (Fig. 6b), a band of maximum convergence is aligned with the upper-level divergence of the SPCZ. Only weak areas of low-level convergence occur near 10°N corresponding to the ITCZ, which is weak during November-February.

4. Vertical Velocity

Vertical velocity (omega) at 400 hPa for December - February is given in Fig. 7. The most prominent bands of maximum rising motion occur along the SPCZ and ITCZ. The SPCZ is most intense and shows a wide band of strong rising motion stretching from north of Australia southeastward to at least 30°S, 135°W.

5. Meridional Cross-Section

A zonal wind cross-section (zonally-averaged between 140°E-180°E) for December-February is given in Fig. 8. At low latitudes, east winds are dominant with maximum low-level easterlies near 10°N. Values approaching -10 m/s occur through the tropical troposphere. It should also be noted that the width of the easterlies does not vary much with height.

IV. DESCRIPTION OF NUMERICAL MODEL SYSTEM

Numerical simulations were performed using the Naval Postgraduate School/Naval Research Laboratory (NPS/NRL) mesoscale numerical weather prediction system. The system is composed of an objective analysis scheme, an initialization scheme, the numerical model, and a diagnostics/visualization package. The formulation of the model is described in detail in Madala et al. (1987), Holt et al. (1990), and Chang et al. (1993). The version of the model used for the present simulations is the 3-D, triply nested, hydrostatic, primitive equation model. Important physical parameterizations in the numerical model include a multi-level planetary boundary layer (PBL), cumulus and stratus parameterizations incorporating an explicit determination of cloud liquid water/ice, and shortwave and longwave radiation.

A. MODEL GRID AND NUMERICS

The nested grid of the model has three horizontal meshes of the Arakawa staggered C-grid centered on the TOGA COARE Intensive Flux Area (IFA) (Fig. 1). The outer coarse grid contains 23 x 18 grid points with a 2.25 deg. lat./long. resolution. The middle grid has 37 x 31 points with 0.75 deg. resolution, and the inner grid has 61 x 49 points with 0.25 deg. resolution. The interaction between the three grids occurs only in one direction (from outer grid inward). As shown in Table 1, the model has 23 sigma layers in the vertical with 15 levels below $\sigma=0.5$.

Integration of the primitive equations is by a spatial finite difference scheme and a split-explicit time integration scheme. The horizontal advection is approximated by a second-order accurate formulation with weak horizontal diffusion ($[K_h \delta x \delta y/dt]=10^{-3}$) of momentum and mass on pressure surfaces to suppress computational noise. A centered leap-frog scheme

Level	$\Delta\sigma$	σ
1	0.1	0.05
2	0.08	0.14
3	0.06	0.21
4	0.06	0.27
5	0.06	0.33
6	0.06	0.39
7	0.05	0.445
8	0.05	0.495
9	0.05	0.545
10	0.05	0.595
11	0.05	0.645
12	0.05	0.695
13	0.04	0.74
14	0.04	0.78
15	0.04	0.82
16	0.04	0.86
17	0.03	0.895
18	0.03	0.925
19	0.02	0.95
20	0.02	0.97
21	0.01	0.985
22	0.005	0.9925
23	0.005	0.9975

Table 1. Vertical grid of the 23-level NPS/NRL model indicating the σ levels (right column) and the thickness $\Delta\sigma$ (center column).

with split-explicit integration (Madala 1978) and a weak time filter (Brown and Campana 1978) are used with time steps of 360, 120, and 40 seconds on the three grids.

B. PHYSICAL PARAMETERIZATIONS

1. Boundary Layer

Parameterizations of mixing in the boundary layer are based upon: (i) similarity theory for the surface layer (represented by the lowest layer of the model with a depth of approximately 20 m) (Monin and Yaglom 1971); and (ii) turbulent kinetic energy (TKE) closure for the mixed layer incorporating budget equations for TKE and dissipation (ϵ) (Holt et al. 1990). The depth of the mixed layer is specified as the uppermost level at which TKE reaches a pre-determined small value (10^{-10} cm^2s^{-2}). A soil slab model is used to predict ground temperature based on the surface energy equation (Blackadar 1976; Chang 1979). Although ocean surface temperature is updated daily from Fleet Numerical Meteorology and Oceanography Center (FNMOC) analyses, no variation of the ocean is allowed during the atmospheric model integration.

2. Convective and Non-convective Condensation

The handling of condensation is one of the most important and difficult tasks facing mesoscale numerical modelers. A variety of approaches for determining both convective and non-convective condensation processes have been proposed. In the NPS/NRL model, parameterizations for both cumulus convection and stratiform condensation incorporate a modification of the scheme proposed by Sundqvist (1988) and Sundqvist et al. (1989). An important feature of the scheme is the explicit determination of cloud liquid water/ice mixing ratio (m). An advantage of this scheme is its relative simplicity--only one additional predictive equation is necessary to represent both cloud water and cloud ice. Since the numerical model does not have an explicit cloud physics component, the microphysical processes of the clouds must be incorporated through additional relationships that simulate the coalescence, Bergeron-Findeisen, and ice crystal diffusion processes. The predictive equation for cloud water/ice is:

$$\frac{\partial m}{\partial t}=A_m+C+Q-P-E_m \ , \qquad (1)$$

where A_m is the tendency of cloud liquid water from all processes other than condensation, C is the net convective rate of release of latent heat, Q is the non-convective rate of release of latent heat, P is the local rate of precipitation, and E_m is evaporation of advected cloud liquid water/ice.

The Sundqvist scheme is general in that any cumulus parameterization can be utilized to partition available vapor into condensate (and associated latent heat release) and a change in relative humidity. For a cloud water scheme, the task is to partition the condensate between cloud water and precipitating water. This task is independent of the choice of cumulus parameterization (Sundqvist 1988). The scheme in Sundqvist et al. (1989) uses a modified version of the Kuo parameterization (Kuo 1965, 1974).

The formation of an upper-tropospheric anvil cloud in the Sundqvist scheme is incorporated by treating the top level of convection with temperatures less than -20°C as stratiform. This represents the simplified communication between convective and non-convective cloud water. Shallow convection is allowed in the model if buoyancy is present averaged over the nearest three model levels above the LCL (Sundqvist et al. 1989).

If a model grid column does not satisfy the criteria for convective condensation, or if convective condensation has not occurred in a "convective" grid cell, a check is performed for stratiform condensation. This latter criterion allows for overlapping convective and non-convective clouds within a grid column. Large-scale condensation is assumed only if relative humidity exceeds a specified threshold value. For a fine-mesh horizontal grid resolution on the order of 25-30 km, the model is unable to resolve explicitly the condensation processes. Hence, the threshold value must be less than unity (Sundqvist et al. 1989). The Sundqvist et al. (1989) parameterization for stratiform cloud cover b_{st} is expressed in terms of this threshold value R_0 and the saturated relative humidity R_s

$$b_{st}=1-\left(\frac{R_s-R}{R_s-R_0}\right) . \tag{2}$$

This scheme specifies a value of R_0 of 0.75 over land and 0.85 over sea. In addition, the profile for R_0 increases linearly with σ to a value near unity at the surface. Model forecasts of precipitation are sensitive to the values of R_0 (Zhao et al. 1991), which is sensitive to model resolution.

Numerical sensitivity tests with this scheme for mesoscale simulations along the west coast of the United States (Ferandez 1993) indicate that the model cloud cover is significantly less than observed in satellite imagery. The discrepancy was due to relatively small R_0 values. Hence, the scheme proposed by Slingo and Ritter (1985) for use in the European Centre for Medium-range Weather Forecasting (ECMWF) atmospheric model is used here instead of the Sundqvist et al. (1989) scheme to determine the threshold relative humidity for non-convective cloud cover

$$R_0=1+2(\sigma^2-\sigma)+\sqrt{3}\,\sigma(1-3\sigma+2\sigma^2) \cdot \tag{3}$$

The convective cloud fraction is determined from the convective rainfall rate P_c (cm h^{-1}) (Slingo and Ritter 1985) as:

$$b_{cu}=\begin{cases}1.13 + 0.124 \ln P_c, & T<233.16°K \\ 0.93 + 0.124 \ln P_c, & T>233.16°K\end{cases} \tag{4}$$

Distinguishing between cloud liquid water and cloud ice follows the scheme of Zhao et al. (1991). For convective condensation, IW=1 (cloud ice) for T<0°C, and IW=0 (cloud water) otherwise. For non-convective condensation, three criteria are considered:

1. for T > 0°C, IW=0
2. for T < -15°C, IW=1
3. for 0°C < T < -15°C, IW=1 if there is cloud ice at or above this grid point at the previous time step; IW=0 otherwise.

In ice cloud regions, the saturation specific humidity is determined with respect to ice, and in water cloud regions it is with respect to water.

Evaluation of the cloud liquid water tendency (1) is by the Newton-Raphson semi-implicit scheme because of the implicit treatment of the P term, while all other terms are treated explicitly. Advection of cloud liquid water is handled by the positive definite, mass conservative scheme of Smolarkiewicz (1983) that minimizes the substantial computational diffusion at cloud edges. Advection of cloud liquid water is calculated only in the horizontal direction, which assumes that an approximate balance exists in the vertical between the gravitational fall velocity of cloud droplets and the upward velocity (Sundqvist et al. 1989).

3. Radiation

The Harshvardhan et al. (1987) broad-band radiation scheme is used to parameterize radiative effects in the numerical model. The scheme provides highly vectorized formulations of emissivity and absorptance of water vapor, ozone, and carbon dioxide to speed computations of radiative processes. Because the radiation routine is highly computationally intensive, it is not called every model time step. A calling interval of every 30 minutes was chosen as a compromise value that would be on the order of the characteristic time scale of cumulus convection.

Longwave fluxes in the cloud-free atmosphere are calculated with the broad-band transmission approach of Chou (1984) for water vapor centered in the 0-340 cm^{-1} and 1380-1900 cm^{-1} bands, Chou and Peng (1983) for carbon dioxide in the band 620-720 cm^{-1}, and Rodgers (1968) for ozone in the 980-1100 cm^{-1} band. A clear line-of-sight probability distribution is used for the cloudy sky from the top of the model to the surface.

Shortwave radiation is parameterized using a basic two-stream method (Lacis and Hansen 1974). Absorption is computed in two wavelength bands ($\lambda < 0.9\mu\mathrm{m}$ and $\lambda > 0.9\mu\mathrm{m}$), where water vapor absorption is dominant in the upper band and ozone in the lower band.

A modification to the Harshvardhan et al. (1987) scheme is the incorporation of cloud optical depth as a function of cloud liquid water mixing ratio. The cloud optical depth τ_d is expressed as a function of liquid water path W (g m^{-2}) and the effective mode radius r (μm) of the cloud droplets

$$\tau_d = 1.5\frac{W}{\rho r}\ , \tag{5}$$

where ρ is the density of condensed water (approximately 1 g cm^{-3}). Liquid water path is computed as (Stephens 1984):

$$W(\sigma,\sigma') = \int_{\sigma}^{\sigma'} m d\sigma\ , \tag{6}$$

where the limits of integration represent cloud base (or top) to a specified depth σ'. The effective mode radius is as prescribed by Charlock and Ramanathan (1985). It is assumed to be a constant 7 μm for cloud layers with temperatures higher than -10°C, 30 μm for cloud layers lower than -30°C, and linearly varying for temperatures between -10° and -30°C.

V. ANALYSIS

This study will consider the distribution of cloud clusters, temperature distribution, and the diurnal variability of different size clusters based upon hourly IR satellite imagery. Then the satellite-observed characteristics of the convection will be compared with the mesoscale model predictions of cloud distribution. The domain for the comparison of the model forecasts will be over the innermost fine mesh only.

A. IR TEMPERATURE THRESHOLDS

This study will use two satellite-derived temperature thresholds to differentiate between cloud types. A threshold temperature of 208°K (-65°C) is used to determine the coldest cloud tops. This threshold is chosen based on the radar echo patterns observed with mature, nocturnal oceanic mesoscale convective systems (MCSs) during the Equatorial Mesoscale Experiment (EMEX) (Webster and Houze 1991; Mapes and Houze 1993).

A temperature of 235°K (-38°C) is chosen as the moderate (lower) cloud temperature. This value has been frequently used in climatic rainfall estimation as an estimator of integrated rainfall amount (Mapes and Houze 1993).

B. DATA AND METHODS

1. Hourly GMS Imagery

As previously described, the satellite imagery is the remapped Japanese GMS IR images on a Mercator projection. The pixel size is 5 km square, with a pixel array of 444 lines by 888 samples (Flament and Bernstein 1993).

A cropped image of the IFA domain was extracted from the full domain. This image is equivalent to the inner grid of the model as shown in Fig. 1 and has 266 lines by 333 samples.

Hourly imagery was collected for two 48-h periods: from 01 UTC 14 January 1993 to 00 UTC 16 January 1993; and from 01 UTC 18 January 1993 to 00 UTC 20 January 1993. Missing images were 19 UTC 18 January and 01-04 UTC 19 January. Linear interpolation between adjacent times was used to fill these gaps. Local time at 150°E is UTC + 10 h.

2. Algorithm

The algorithm used to determine cloud clusters in this study is based on that used by Wielicki and Welch (1986) and is similar to another developed by Williams and Houze (1987). The cloud cluster analysis is accomplished with a single pass through the satellite data, starting at the top of the image, and scanning three lines of pixels at a time. Cloud pixels are grouped into segments within the scan line. A cloud segment is a group of cloud pixels with clear pixels on its right (east) and left (west) sides. As the scan continues, pixels in the previous scan line can be flagged as clear, cloud edge, or cloud interior. As long as cloud segments remain distinct, they can be considered as separate clouds. Cloud segments in adjacent scan lines are joined as the analysis moves through the image. Cloud cluster area is determined as the number of cloudy pixels multiplied by the pixel area.

C. PERIOD OF STUDY

The two 48-h periods were chosen for differences in breadth and type of convection. A brief description of conditions observed from enhanced GMS satellite imagery (Figs. 9-18) during these two periods follows. The cloud temperatures less than 208°K are shown in white. Cloud top temperatures less than 235°K but higher than 208°K are shown with a color spectrum. Finally, temperatures higher than 235°K fade gradually from white to black. It should be noted that temperatures less than 193°K were clipped from the imagery and will show up as black embedded in the cold (less than 208°K) white areas.

1. 14-15 January 1993

The IFA area on 14-15 January (Figs. 9-13) is characterized by mostly clear conditions to the south with a band of deep convection moving into the IFA from the north and east (Fig. 9). This convective band is consistent with the January climatological position of the ITCZ as discussed in Chapter III. However, it appears stronger than the characteristically weak January ITCZ (see Fig. 6). From the 14th to the 15th (Figs. 10-13), the ITCZ cloud band moves to the southwest and then dissipates, with minimum coverage around 0145 UTC (1145 local) on the 15th (Fig. 11). By 1945 UTC (0545 local) 15 January, convective bands associated with the ITCZ are reforming along approximately 3°N in the IFA. By 2345 UTC (1045 local) 15 January (Fig. 13), this convection is stronger and again atypical of ITCZ conditions for January.

2. 18-19 January 1993

In contrast to 14-15 January, 18-19 January (Figs. 14-18) is characterized by widespread and seemingly disorganized convection. No confined convergent zone is apparent in the form of convective banding during this period. Initially, this widespread convection (Fig. 14) is apparent throughout the IFA and becomes even more widespread by 1145 UTC (2245 local) 18 January (Fig. 15). In the early morning hours (Fig. 16), deep, yet sporadic convection once again appears. This convection includes a fairly large, but short-lived, Mesoscale Convective System (MCS) located on the eastern edge of the IFA. By 1145 UTC (2145 local) 19 January (Fig. 17), the MCS has broken up with the remaining clouds moving west, into the center of the IFA. Finally by 2045 UTC (0645 local) 19 January (Fig. 18), an increase in deep convection has occurred along the SPCZ with some clearing on the eastern edge of the IFA. This less organized regime of convection is more typical of January climatology as depicted in the previous chapter, and with the convergence/divergence pattern in the region of the IFA depicted in Fig. 6.

D. CLUSTER SIZE DISTRIBUTIONS

The frequency distribution of cloud shield sizes using a threshold of 208°K for all the hourly data during 14-15 and 18-19 January is shown in Fig. 19. Data from the full domain (31,769 data points) and the IFA domain (14,339 data points) are overlaid. As found with previous studies of cloud cluster size distributions, a near log-normal distribution is evident. Notice that the cluster distribution in the IFA domain is also representative of the distribution in the full domain. About 30% of cloud clusters are smaller than 30 km^2, 50% are smaller than 80 km^2, and 90% are smaller than 3000 km^2. The cloud shield sizes in this frequency distribution are smaller than found by Mapes and Houze (1993) who analyzed data from three consecutive November-February periods from 1986 until 1988 using the same cloud shield algorithm. Whereas this study is for the smaller TOGA-COARE domain, the Mapes and Houze (1993) study encompassed most of the tropical western Pacific. This may partially account for why the cloud shield distributions for the two studies are different. Chen et al. (1993) noted that mid-January of the TOGA-COARE period generally had suppressed convection, which may also partially account for the differences in cloud shield size.

Cumulative fractional area coverage with increasing cluster size is depicted in Fig. 20 for all days of the study. After dividing the sample into quartiles, the four cloud cluster size ranges are named for convenience: small, medium, large, and giant (Mapes and Houze 1993). Each quartile contributes an equal amount to the total area of cloud top colder than the indicated temperature. These cluster size ranges for the 208°K and 235°K thresholds for the entire sample are shown in Table 2, and separately for the two 48-h time periods in Table 3.

	Small (km^2)	Medium (km^2)	Large (km^2)	Giant (km^2)
208°K	< 7800	< 24,000	< 62,000	> 62,000
235°K	< 27,000	< 104,000	< 235,000	> 235,000

Table 2. Cloud cluster size ranges for all study days.

	Small (km^2)	Medium (km^2)	Large (km^2)	Giant (km^2)
14-15 Jan				
208°K	< 2200	< 8800	< 24,000	> 24,000
235°K	< 16,000	< 46,000	< 133,000	> 133,000
18-19 Jan				
208°K	< 8800	< 28,000	< 65,000	> 65,000
235°K	< 37,000	< 146,000	< 345,000	> 345,000

Table 3. Cloud cluster size ranges for separate 48-h periods.

Table 2 indicates that the cluster size ranges are about four times larger for the 235°K threshold than for the 208°K threshold. During this period, the largest 235°K cluster found is nearly four times the size of the largest 208°K cluster. Table 3 indicates that this cluster size difference is less for 14-15 January, and greater for 18-19 January. This indicates more convection during 18-19 January.

E. DIURNAL CYCLE

It is important to understand that meaningful statistical conclusions concerning a diurnal signal cannot be generalized from the small sample examined in this case-study. The purpose here is to examine the two specific 48-h time periods, and determine the diurnal variability (if any) for these periods alone and to compare with model forecasts. The model forecasts will be presented in the next chapter.

Figs. 21 and 22 illustrate a 48-h time series of pixel percentages with IR temperatures below the thresholds of 208°K and 235°K for January 14-15 and 18-19 respectively. As described previously, 14-15 January is a period characterized by an extension of the ITCZ into the IFA domain, the subsequent collapse of convection, and finally the rebuilding of the ITCZ. This sequence of events is readily apparent in Fig. 21. High percentages of cold pixels (corresponding to greater area of cold clouds) dominate early on the 14th (Fig. 9). The cold area drops to a minimum by 0200 UTC (1200 local) 15 January (Fig. 11), and peaks again by 0000 UTC (1000 local) 16 January (Fig. 13). Diurnal variability is much smaller than the synoptic-scale variability. Small local peaks in the 235°K curve do occur at 1600 local and 0100 local during the first 24-h period, and peaks occur at 1700 local and 0600 local during the second 24 hrs.

For the period 18-19 January (Fig. 22), a larger diurnal variability is apparent, particularly for the 208°K threshold. Beginning with a relative minimum near 1200 local (see Fig. 14), the percent of cold cloud area increases to a relative maximum at 0600 local (Fig. 16) for both 208°K and 235°K. Then decreases in the cold area for 208°K occur until a minimum is reached at 1800 local (Fig. 17). However, a peak for the 235°K occurs at 1500 local. Both the 208°K and 235°K curves reach a relative maximum at 0600 local (Fig. 18) the next morning. Thus, the 18-19 January period has relative maxima for the colder cloud tops before sunrise, and a secondary maximum in the moderately cold tops (<235°K) in the mid-to-late afternoon (1500-1800 local). Whereas 15 January tends to have a similar diurnal evolution, it is obscurred by the trend associated with synoptic-scale variability.

The dependency on cloud cluster size for the diurnal signal of total cloud coverage is illuminated in Figs. 23 and 24. The means of the accumulated cloud cluster areas for the two 48-h time periods have been removed. The large cold cloud area from 1100 local 14 January to 0700 local 15 January observed in Fig. 21 is associated with an accumulation of the cloud cluster sizes evident for the same time period in Fig. 23. However, large and giant clusters seem to be slightly more prevalent. Small clusters are most common during the minimum around 1000 local 15 January. Between 0100 - 0900 local 15 January, all of the cluster sizes seem to contribute to the cold cloud area. However, the prominent early morning (0500 local) peak is due to giant clusters.

For 18-19 January (Fig. 24), a much stronger diurnal signal for the giant clusters is present compared to 14-15 January, with the maxima occurring from 0600-1000 local. The small, medium and large clusters tend to peak slightly earlier (0000-1000 local). Local minima for all cluster sizes occur near 1600 local on both the 18th and 19th.

Grey-shaded contour plots of hourly histograms of cloud top temperatures within 1°C intervals between 0°C to -91°C are shown in Figs. 25 and 26. These plots were produced by taking the black body temperature value of each pixel from the hourly IR images of the IFA domain, and evaluating whether it is within 1°C (± .5°C) of each degree of temperature from 0°C to -90°C on the plot. To distinguish a diurnal signal from this data, a mean value for the 235°K area of coverage for each day is then determined. Then for each hour, the percentage of that mean area made up by each temperature value is calculated. The values are then normalized to 235°K (-38°C). The units of the plotted field is percent of daily mean 235°K coverage per degree. The highest percentages (brightest values in the plots) indicate a maximum for each temperature indicated, and a time evolution of convection at specific temperatures (i.e., levels) can be observed.

During 14 January (Fig. 25), the coldest clouds (less than -60°C) dissipate from 1000-1800 UTC (2000-0400 local), before the warmer (lower) clouds have reached their maximum (note the downward tilt of relative maxima indicated during the 14th in Fig. 25). This 'slumping effect' is related to the late night/early morning deep convection collapsing and spreading out horizontally (Mapes and Houze 1993).

During 15 January (Fig. 25), a strong maximum in very cold cloud tops suddenly erupts in the early morning hours (near 0600 local). Moreover, the warmer cloud top temperatures also increase suddenly during the early morning hours of the 15th.

Although the slumping effect is not quite as noticeable during 18-19 January (Fig. 26), a strong diurnal signal is evident in the moderately cold clouds (warmer than -38°C) with a strong late afternoon and early evening maximum. Albright et al. (1985) suggested that this afternoon peak was representative of a "second regime of less deep convection." That is, the less deep convection may have a different diurnal variability than the very cold cloud-top temperatures that occurred in the early morning hours of the 19th. It is also possible that this afternoon maximum is a result of secondary convection triggered by the outflows from the deeper early morning convection.

To examine the evolution of the different cloud cluster sizes within these time/height cross sections, contour plots similar to Figs. 25-26 are constructed for the four 235°K cloud cluster sizes (Figs. 27 and 28). The plots are given for each of the four days of this study in order to closely examine the diurnal evolution. Note that only temperatures lower than -38°C (235°K) are represented on the vertical scale because only these colder temperatures lie within the 235°K cloud clusters.

For the 14th and 15th, the only small clusters occur from 1200-1800 local (Fig. 27a). However, the medium and large (mesoscale) size clusters (Figs. 27b-c) contribute the most to the cycle with peaks in the afternoon and early morning. This is in agreement with the results of Mapes and Houze (1993). The giant clusters are present in the afternoon and early evening of the 14th, and at 0500-0900 local on the 15th (Fig. 27d). Because there is little day-to-day consistency for any of the cluster sizes depicted in Fig. 27, it is evident that synoptic-scale variability is overwhelming any obvious diurnal signal during 14-15 January.

The small clusters on the 18th and 19th (Fig. 28a) only occur from mid-morning to around noon local time on the 19th. The medium and large clusters contribute to both the morning and afternoon maxima (Figs. 28b-c). The giant clusters contribute most to the early morning peak of the 20th (Fig. 28d).

This case study confirms that the diurnal variability of convection is more complex than a simple 24-h maximum and minimum. For example, the cases examined in this study do not always display an early morning maximum. In studies with greater temporal, as well as spatial coverage, this early morning maximum is evident as a seasonal (Northern Hemisphere winter) average (Gray and Jacobson 1977; Albright et al. 1985; Mapes and Houze 1993). Warmer clouds exhibit a large diurnal variation, but with peaks in the late afternoon and early evening. Thus, this small sample is consistent with a scenario of very deep clouds building through the night and reaching a peak before sunrise, and less deep clouds that increase through the daytime and reach a peak in the late afternoon or early evening.

This idealized scenario is more evident during the period of 18-19 January than during 14-15 January. Here, the complexity of studying diurnal convective variability as a mesoscale process is complicated by the presence of large-scale convergence with the encroachment of the ITCZ into the IFA. The added complexity of energy conversion and interaction between large (synoptic) scales and smaller (meso) scales disrupts the diurnal convective signal.

F. MODEL VERIFICATION

Model runs were conducted for both of the 48-h periods with a run beginning at 0000 UTC on the 14th and 18th respectively. Model verification will be in four areas: (i) cloud cover; (ii) cluster size distributions; (iii) cluster diurnal cycle; and (iv) atmospheric vertical structure.

1. Cloud Cover

No special initialization of the model cloud cover is included in the model physics. Thus, the large-scale forcing, including air-sea fluxes, must generate the cloud cover during the integration. Total cloud cover is calculated by a combination of the stratus cloud fraction (Eqn. 2) and the convective cloud fraction (Eqn. 4) assuming independent probabilities

$$b=b_{st}+b_{cu}-b_{st}b_{cu} \quad . \qquad \textbf{(7)}$$

The resulting two-dimensional fractional cloud cover b^* is computed assuming random or maximum overlap of individual cloud fractions (b) within a grid column over all model levels (i.e., j=1 to 23) (Sundqvist et al. 1989):

$$b^{*}=1-\pi\left[1-\max(b_{j-1},b_{j})/(1-b_{j-1})\right] \quad . \qquad \mathbf{(8)}$$

For a column cloud cover monotonically increasing or decreasing with height, maximum overlapping occurs ($b^{*}=\max b_j$). Random overlapping occurs for a non-monotonic change with height, which results in a larger b^{*} than the maximum of b_j. This fractional cloud cover field b^{*} can then be compared to satellite-observed cloud cover.

Model forecasts of total cloud cover for the IFA domain are depicted in Figs. 29 and 30. Dotted shading represents 50-75% cloud cover, and hatched shading represents greater than 75% cloud cover. These forecast fields will be compared with the corresponding red boxed IFA domain on the satellite imagery in Figs. 10-13 for 14-15 January and Figs. 15-18 for 18-19 January.

a. 14-15 January

The 9-h forecast total cloud cover field (Fig. 29a) does predict the majority of cloud cover would be north of the equator in the IFA domain. South of the equator is mostly clear with the exception of clouds over New Britain and New Ireland in the southwest. The corresponding satellite image (Fig. 10) depicts a heavy band of clouds north of the equator, but not the large area of clouds the model has predicted in the northwest corner. The clouds over the islands are also verified.

Although the 24-h forecast (Fig. 29b) shows a continuation of the cloud cover north of the equator, the area of >75% coverage has decreased. Increased scattered cloudiness is predicted south of the equator. The corresponding image (Fig. 11) has greatly decreased cloudiness to the north and nearly clear conditions to the south of the equator.

The 36- and 48-h forecasts (Figs. 29c-d) depict nearly uniform scattered cloud cover over the entire IFA domain. The corresponding imagery (Figs. 12 and 13) shows a dramatic increase in the cloud band north of the equator with continued clear conditions to the south. Overall, the model shows some skill in its cloud cover forecasts for 14-15 January out to 24 h. However, the 36- and 48-h forecasts are much less realistic.

b. 18-19 January

The 12-h forecast from 0000 UTC 18 January of total cloud cover (Fig. 30a) predicts 50% or greater coverage over most of the IFA domain with scattered areas of greater than 75% coverage. This agrees with the general pattern of scattered clouds throughout the domain as depicted by the corresponding satellite image (Fig. 15), although the image depicts a nearly clear band near the center of the domain.

The 21-h forecast (Fig. 30b) predicts some clearing to the north but otherwise continued greater than 50% coverage over a band through the center of the domain. The satellite image (Fig. 16) also has clearing in the north as well as in the northwest of the domain. However, a large area of deep convection has developed in the center of the domain that has been missed by the model.

The forecast fields for 36 and 45 h (Figs. 30c-d) show generally scattered cloud cover over the entire domain. The corresponding imagery (Figs. 17 and 18) depict continued deep convection in the center of the domain with clearing to the east in the latter image.

Again, the model shows some forecast skill early in the model integration, although the development of the deeper convective area (Fig. 16) was missed.

2. Cluster Size Distributions

Fig. 31 is a distribution of the model's cloud fraction versus accumulated frequency for all days in the study over the inner mesh of the model. In this figure, the model's 50% and 70% grid-volume cloud fraction thresholds are compared with the 235°K IR satellite distribution. The cloud clusters for the model were calculated in the same manner as were the satellite cloud clusters. The cloud shield sizes for the model are larger for each frequency of occurrence. For example, at a 50% model cloud fraction threshold, 90% of the model cloud clusters are less than 14,000 km^2. At a 70% model threshold, 90% of the model clusters are less than 11,500 km^2. The satellite 235°K distribution has 90% of the cloud clusters only up to 1150 km^2. Part of this difference could be due to the difference in resolution between the model and the 5 km^2 pixel resolution of the satellite sensor. That is, the model can resolve clouds greater than (25x25) km^2, but must parameterize clouds of smaller size.

Fig. 32 is a cumulative fraction versus the 50% and 70% model cloud fraction distribution for all four days of the model run. The 235°K satellite cloud cluster distribution values are overlaid. The model cluster categories are generated in the same manner as the satellite clusters by dividing the cumulative fraction into quartiles, each contributing an equal amount to the total area of cloud top defined by each threshold. Whereas half of the 235°K cloudiness is in clusters larger than 10^5 km^2, half of the 70% model threshold cloudiness is larger than 2 X 10^5 km^2, and the 50% model threshold cloudiness is larger than 6 X 10^5 km^2. The cluster size ranges of the model, using the 70% cloud fraction threshold, for the two 48-h periods are given in Table 4. It is evident that the model is over-forecasting the cluster sizes as the cluster ranges are larger than those of the satellite-analyzed 235°K clusters in Tables 2 and 3 for all cases. The increasing trend in the 235°K values shown in Table 3 for cluster sizes of 14-15 January compared to 18-19 January is also evident in the small and medium model cluster sizes in Table 4, which is evidence of some forecast skill of model cluster size growth.

	Small (km^2)	Medium (km^2)	Large (km^2)	Giant (km^2)
14-15 Jan	<36,000	<173,000	<460,000	>460,000
18-19 Jan	<47,500	<191,000	<450,000	>450,000

Table 4. Model cluster size ranges (70% cloud fraction).

3. Cluster Diurnal Cycle

Figs. 33 and 34 are the 48-h time series of the model's deviation of accumulated area for 14-15 January and 18-19 January, respectively. These are the deviations from the mean areal coverage for each of the cluster size categories that are defined in Table 4. These curves are based on interpolated model output every 3 hours.

During the first 48-h period (Fig. 33), the model appears to have a diurnal signal in the large cluster sizes, with maxima at 1800 UTC (0400 local) on the 14th and at 1500 UTC (0100 local) on the 15th. This somewhat approximates the variations in the satellite-derived large cluster sizes (Fig. 23), although the satellite maxima occur at 1100 UTC (2100 local) on the 14th and at 2100 UTC (0800 local) on the 15th. There is a less clear signal for the small- and medium-size clusters. The model shows a near-constant increase in the giant cluster size.

For 18-19 January (Fig. 34), the model has a maximum in large cluster sizes at 1500 UTC (0100 local). This is near the satellite-derived local maximum for the 18th (Fig. 24). Again, there is a near constant increase in the giant clusters during the period. Otherwise, there is no clear diurnal signal in the model data for this period.

4. Atmospheric Vertical Structure

The soundings were taken during the IOP from the island and ship locations illustrated in Fig. 1. Validation of model vertical structure for the same locations is accomplished through comparison with skew-T log-p depictions of available soundings. The model soundings at the closest grid point was used to avoid horizontal interpolation. Specific soundings were chosen for their location in or near a cloud shield. Environmental soundings and model soundings are compared in a subjective manner, concentrating on the moisture conditions in the lower, middle, and upper troposphere, and wind structure from the surface to 200 mb. The model's top two levels are at 200 and 100 mb.

a. 14 January 1993 0500-0600 UTC (1500-1600 local).

Kavieng is located under a small cloud mass that is probably topographically/heating induced. Low-level moisture is reflected by both the model and sounding (Fig. 35a-b). However, the model tends to dry out too quickly in this 6-h forecast. The model is also much too moist in the upper troposphere. The wind structure is depicted quite accurately by the model with southerly winds at the surface, backing with height to northeasterly near 200 mb.

b. 14 January 1993 1100-1200 UTC (2100-2200 local).

Kapingamaranji is located on the southwestern edge of a giant, very cold (208°K) cloud mass associated with the ITCZ. The model 12-h forecast shows a low-level deck to a greater extent than the environment (Fig. 36a-b). The model dries out similar to the environment through the mid-troposphere. The model does not reflect a dry upper-troposphere as depicted in the environmental sounding. The model shows consistent easterly winds through the mid-troposphere. Although this is somewhat consistent with the environment, the environmental winds are not as uniform. Again, the model accurately backs the winds in the upper troposphere.

c. 15 January 1993 1100-1200 UTC (2100-2200 local).

R/V Shiyan 3 (XP3) is located in a small, moderately cold (<235°K) cloud cluster. In this case (Fig. 37a-b), an excellent depiction of the environmental sounding is achieved by the model 36-h forecast. A low-level cloud deck is depicted accurately, along with mid-level troposphere drying and a moist upper troposphere. The winds are depicted quite accurately with easterly surface winds backing to westerly with height.

d. 15 January 1993 1200 UTC (2200 local).

Kapingamaranji is located in a small, moderately cold (<235°K) cloud cluster. Although a low-level cloud deck is predicted by the model 36-h forecast, it is not nearly as deep a cloud layer as shown by the environmental sounding (Fig. 38a-b). A dry mid-troposphere is depicted well. The model has a more moist upper level than the environment. The wind structure is accurate through the mid-troposphere, with easterly winds at the surface backing to northwesterly at 200 mb. However, the environment has westerly winds above 400 mb.

e. 18 January 1993 1100-1200 UTC (2100-2200 local).

The R/V Shiyan 3 (XP3) is located in a large moderately cold (235°K) cloud mass. The environmental sounding has a deep cloud layer through the mid-troposphere with a fairly moist upper level (Fig. 39a-b). The model 12-h forecast depicts a low-level deck with moderate to dry moisture values through the upper troposphere. The winds are backed accurately from easterly at the surface to westerly in the upper troposphere.

f. 18 January 1993 1700-1800 UTC (0300-0400 local).

Manus is located in a large moderately cold (235°K) cloud mass. The environmental sounding depicts this cloud mass as being mostly mid-tropospheric. The model 18-h forecast does a reasonable job in depicting this, although the model is not as moist as the environment (Fig. 40a-b). The winds are not depicted accurately. Whereas the environment has northerly winds at the surface backing to southerly winds at 200 mb, the model has southerly winds at the surface backing to easterly at 200 mb.

g. 19 January 1993 1100-1200 UTC (2100-2200 local).

R/V Kexue 1 (SC1) is located in a large moderately cold (235°K) cloud mass. The environmental sounding depicts a deep cloud layer through most of the troposphere. The model 36-h forecast depicts a possible low-level cloud deck with a relatively dry troposphere from about 900 mb to 500 mb (Fig. 41a-b). The environment has southeasterly winds at the surface backing to westerly by 600 mb. The model has northeasterly winds at the surface, backing to westerly by 400 mb, then veering to northerly through 200 mb.

h. 19 January 1993 2300-0000 UTC (0900-1000 local).

R/V Kexue 1 (SC1) is located in a giant, very cold (208°K) cloud mass. Similar to the previous sounding, the environment shows a very deep, moist cloud layer. The model 48-h forecast has a much drier lower troposphere as well as surface layer (Fig. 42a-b). The environment has easterly surface winds veering to southerly by the mid-troposphere and through 200 mb. The model has southeasterly winds at the surface and westerly winds at 500 mb that then veer to northerly by 300 mb.

It should be noted that it is difficult to represent a single point accurately from model output and then compare the output with a point source observation such as a sounding. For example, the grid point chosen for the model sounding may be unsaturated when an adjoining grid point is saturated.

The model seems to predict the atmospheric vertical structure best for areas of more organized convection and larger cloud shield sizes. In most cases, the model seems to have little difficulty in picking up the climatological wind profile for the TOGA region of easterly winds at the surface, backing to westerly winds aloft. However, the wind strength and direction at individual levels is sometimes poorly predicted.

The model's overall performance was better for the 14-15 January period than for 18-19 January. The presence of a more discernable synoptic pattern, specifically the presence of an obvious ITCZ during 14-15 January, allowed the model to better describe the cloud pattern and atmospheric structure during this period. The more varied and less organized convection during 18-19 January was forecast less well by the model.

VI. SUMMARY

A. CONCLUSIONS

The analysis of the IR satellite imagery for the two 48-h hour periods revealed that the cluster size distributions were much smaller than for those of seasonal studies conducted by Mapes and Houze (1993). During 14-15 January, the synoptic-scale variability seems to be obscurring much of the diurnal signal. However, the diurnal signal for 18-19 January is more evident with relative maxima in colder (208°K) cloud tops before sunrise and secondary maxima in the moderately cold tops (235°K) in the afternoon and early evening.

For the two 48-h time periods of the study, the model shows some skill in the forecast of total cloud cover. However, the forecasts only appear valid out to about 24 h. It is evident that the model is over-forecasting the size of the cloud clusters as compared to that observed from satellite imagery. The model also failed to indicate a clear diurnal signal during the periods of the study. Limitations in model initialization, and specifically in the initial cloud conditions, contribute to this failure. Also a sea-surface temperature that is updated daily lacks the temporal resolution necessary to contribute any diurnal forcing to the model.

B. RECOMMENDATIONS FOR FURTHER STUDY

It is necessary to examine a larger sample of satellite imagery to better document the diurnal variation in convection. This would allow a more statistically meaningful measure of the diurnal signal.

Because the diurnal signal is small compared to synoptic variability, a prediction model can be at a disadvantage in discerning the diurnal signal because of temporal and spatial model resolution limitations. In addition, the problem of how to analyze and input the initial cloud conditions for the model, i.e., "cloud-spinup", is considerable. Further study in this initialization problem, as well as some investigation as to whether the deep convection is being forced by mesoscale processes not contained in the initial fields of the model, would be beneficial. Further investigation into the prediction of extensive stable cloud decks with radiative feedback is required. Finally, the influence of mesoscale variation in the ocean-surface temperature during model integration would be of interest.

APPENDIX. FIGURES

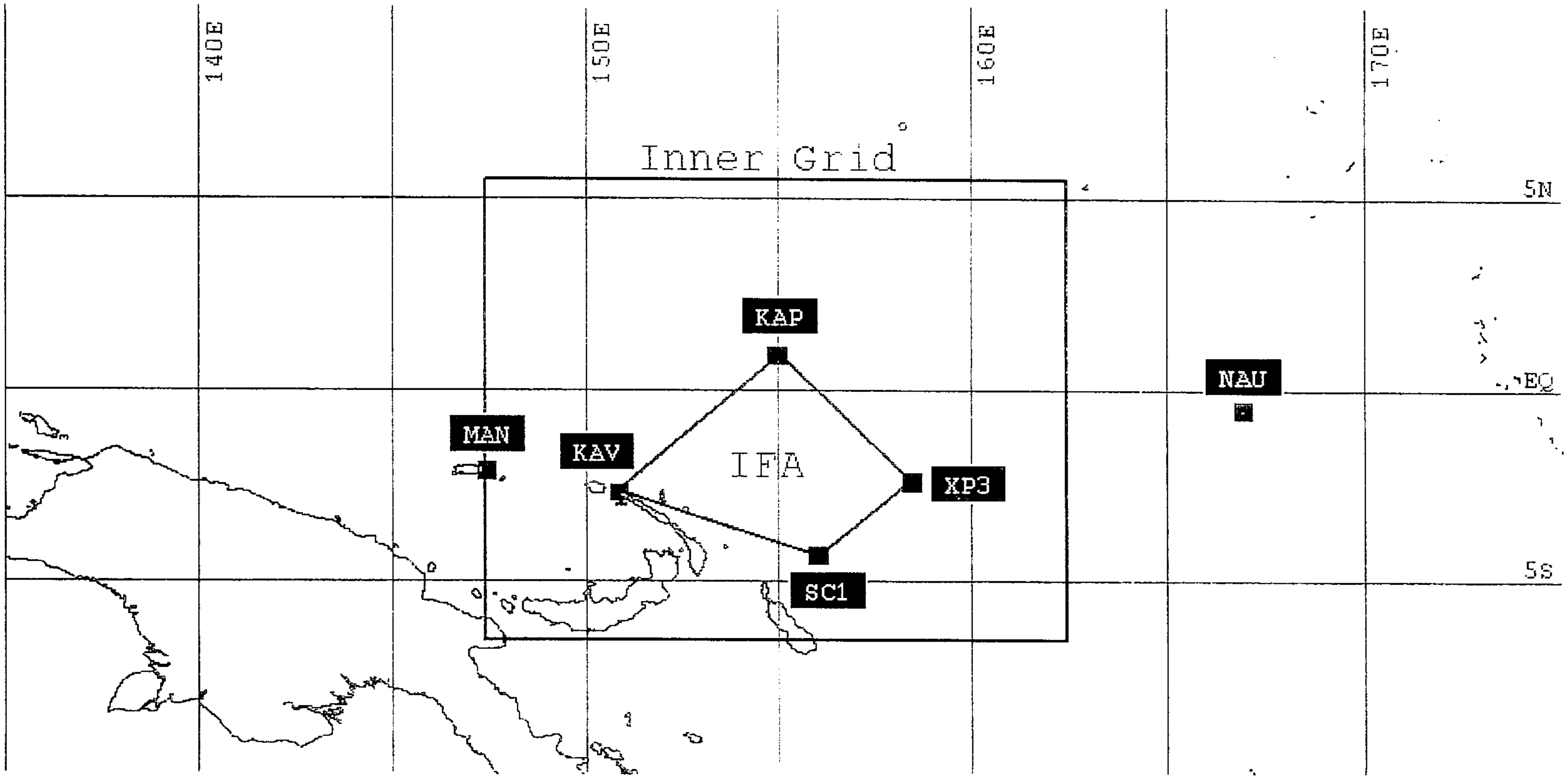

Figure 1. Base map of the TOGA-COARE LSA. The IFA and associated observing stations are illustrated in blue. The inner grid of the model is indicated by the red box.

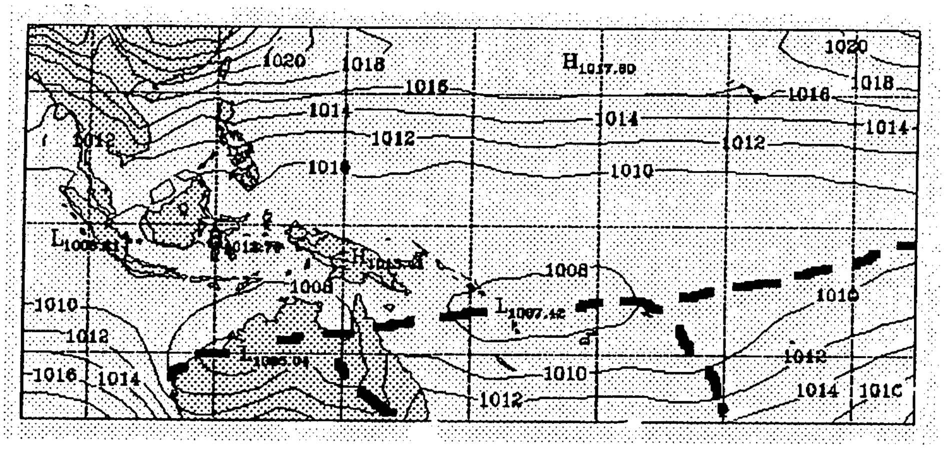

Figure 2. Average mean sea level pressure in hPa for January.
Axes of low pressure troughs are dashed. (From Fig. 2 of Schrage and Vincent 1993).

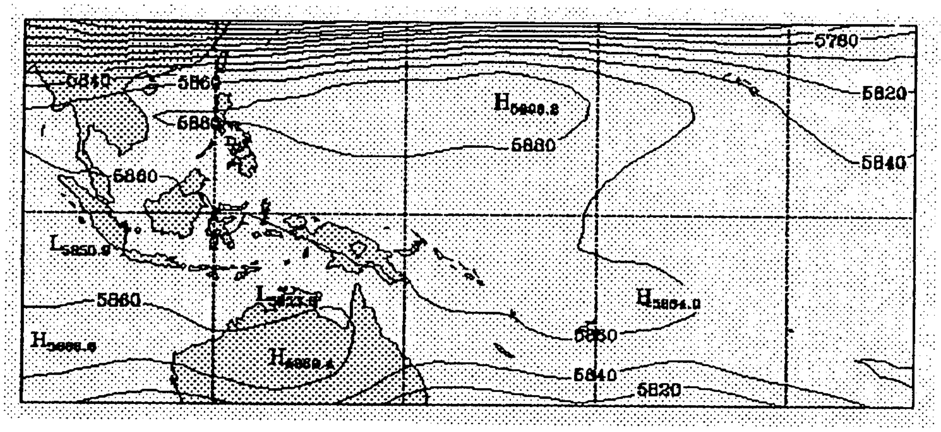

Figure 3. Average geopotential height at 500 hPa in meters for January. (From Fig. 4 of Schrage and Vincent 1993).

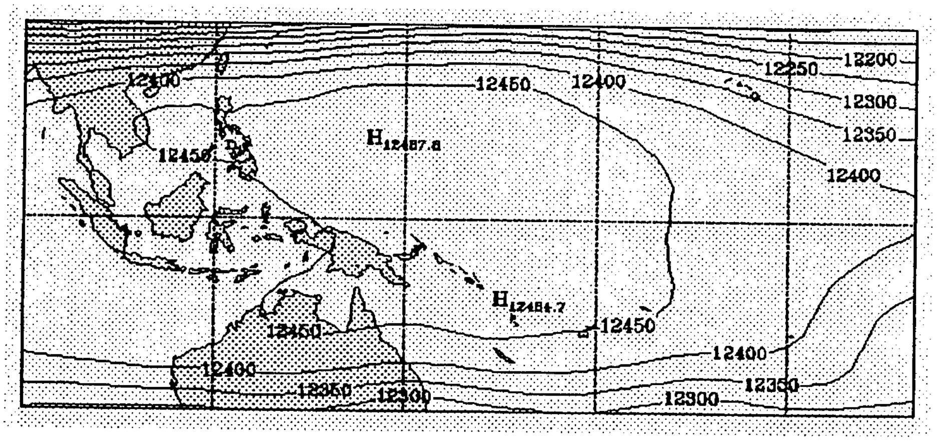

Figure 4. Average geopotential height at 200 hPa in meters for January. (From Fig. 6 of Schrage and Vincent 1993).

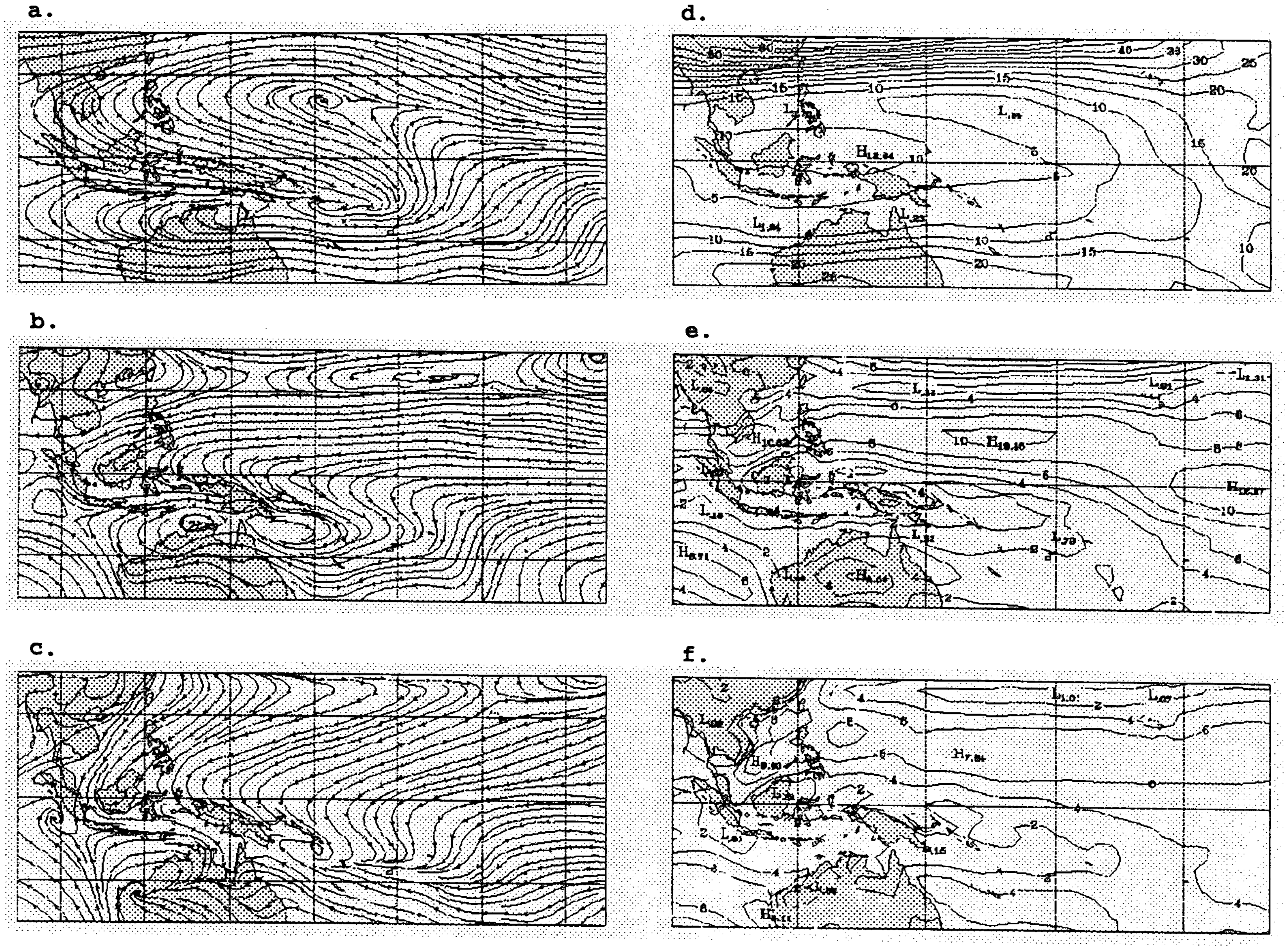

Figure 5. Average streamlines at (a) 200 hPa, (b) 850 hPa, (c) surface and average isotachs in m/s at (d) 200 hPa, (e) 850 hPa, and (f) surface for January. (From Fig. 8 of Schrage and Vincent 1993).

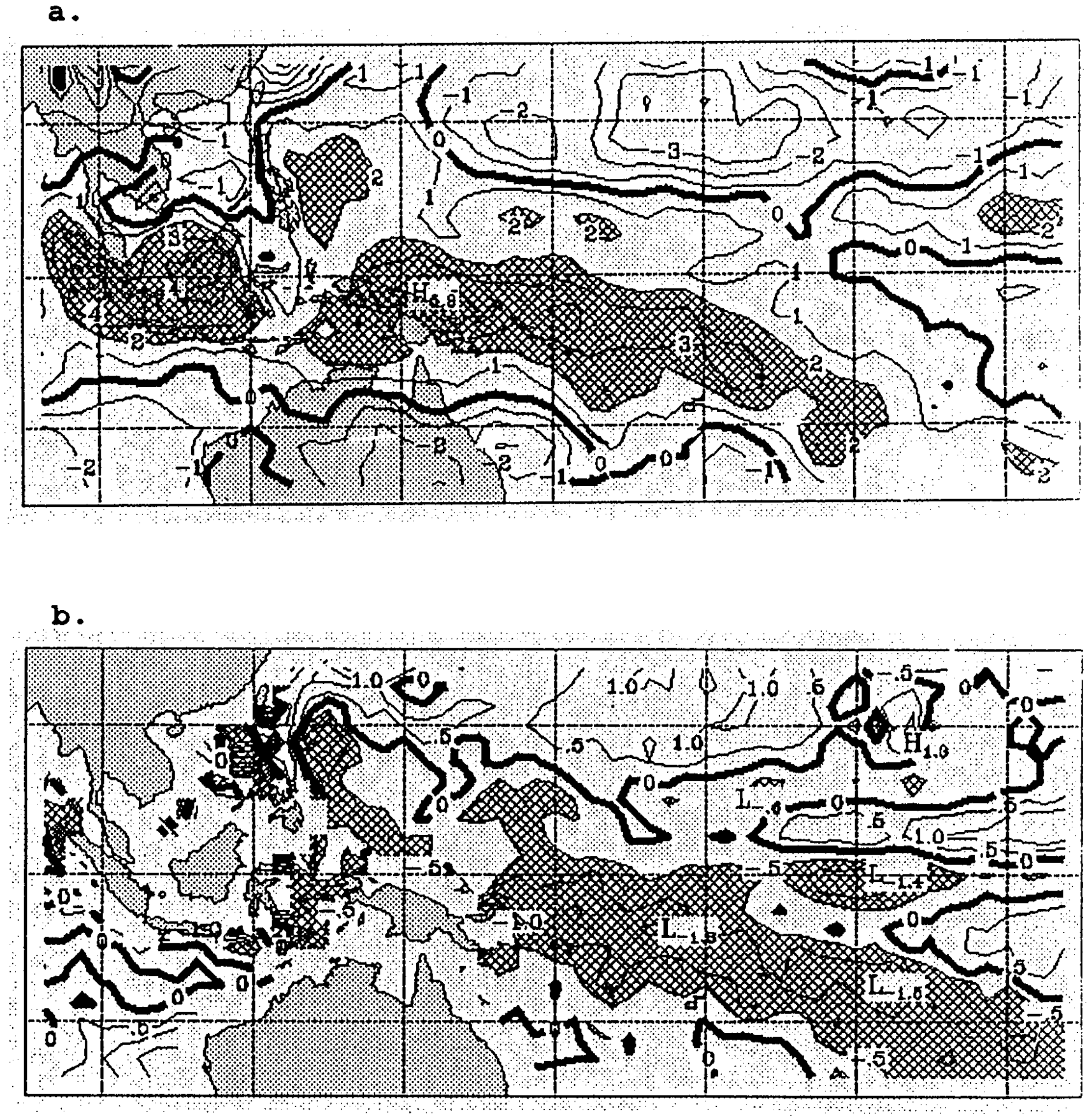

Figure 6. Average horizontal divergence for the 4-month season, November-February, in 10^{-6}/s at (a) 200 hPa with values $\geq 2\text{X}10^{-6}$/s shaded and (b) 850 hPa with values $\leq -0.5\text{X}10^{-6}$/s shaded and analysis over land areas suppressed. (From Fig. 39 of Schrage and Vincent 1993).

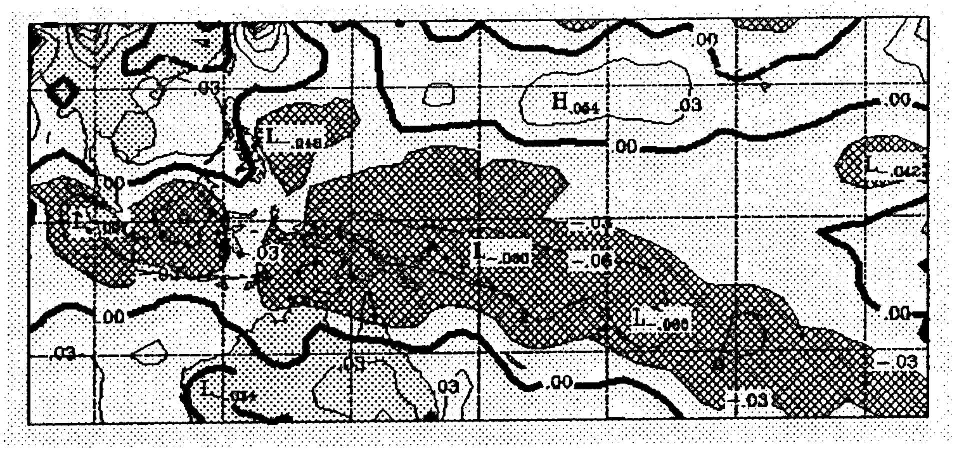

Figure 7. Average vertical velocity in Pa/s at 400 hPa for December-February. (From Fig. 40 of Schrage and Vincent 1993).

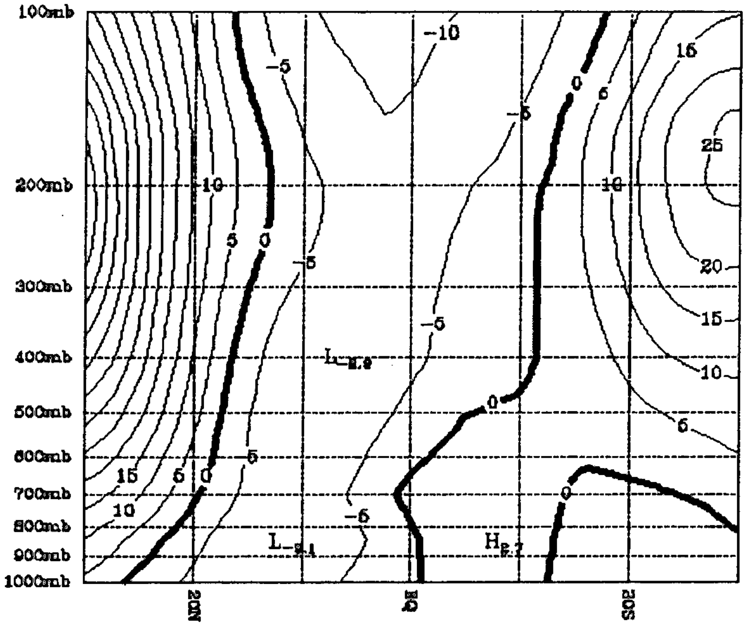

Figure 8. Meridional cross-section of zonal wind in m/s, averaged between 140°E and 180°E for December-February. (From Fig. 52 of Schrage and Vincent 1993).

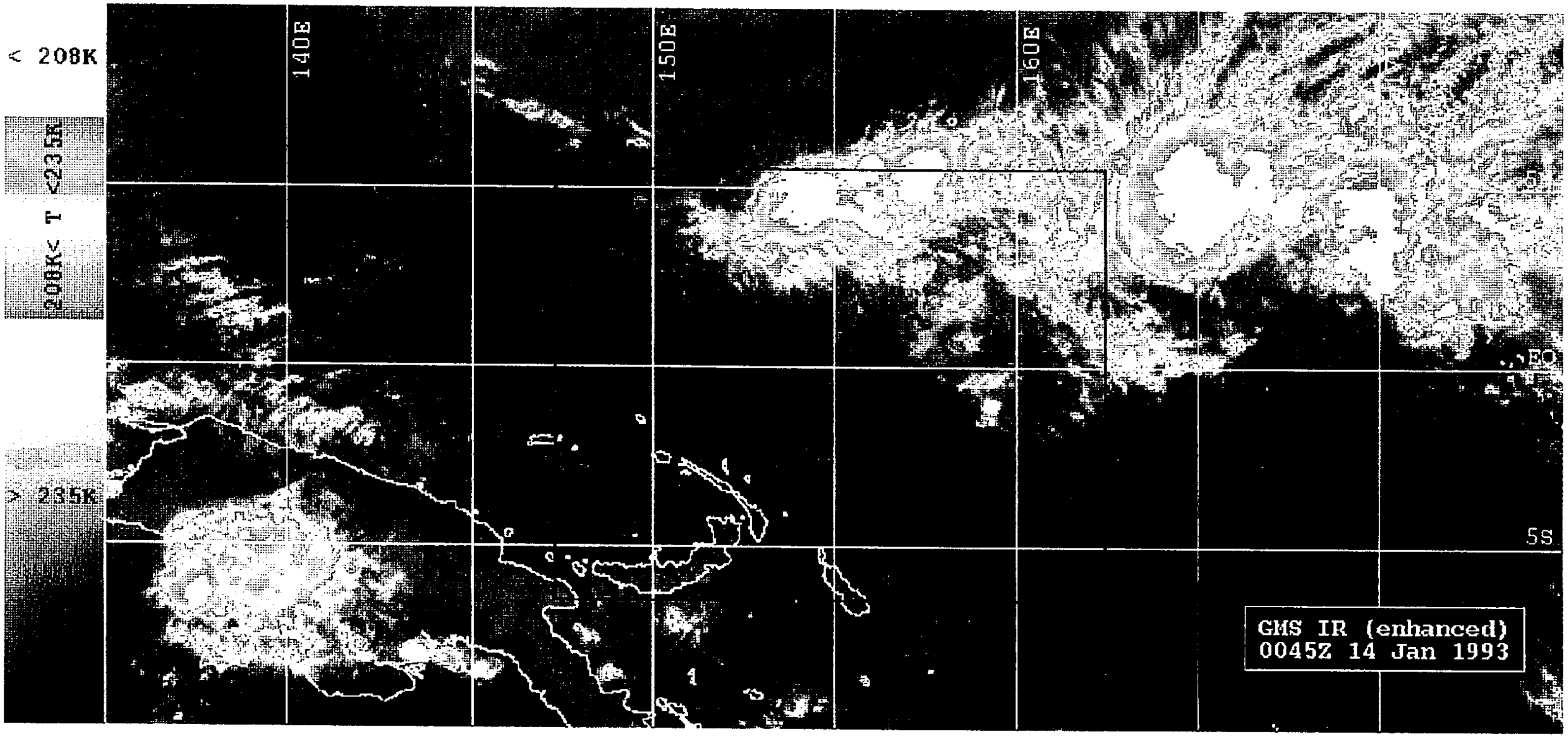

Figure 9. GMS IR image for 0045 UTC 14 January 1993.

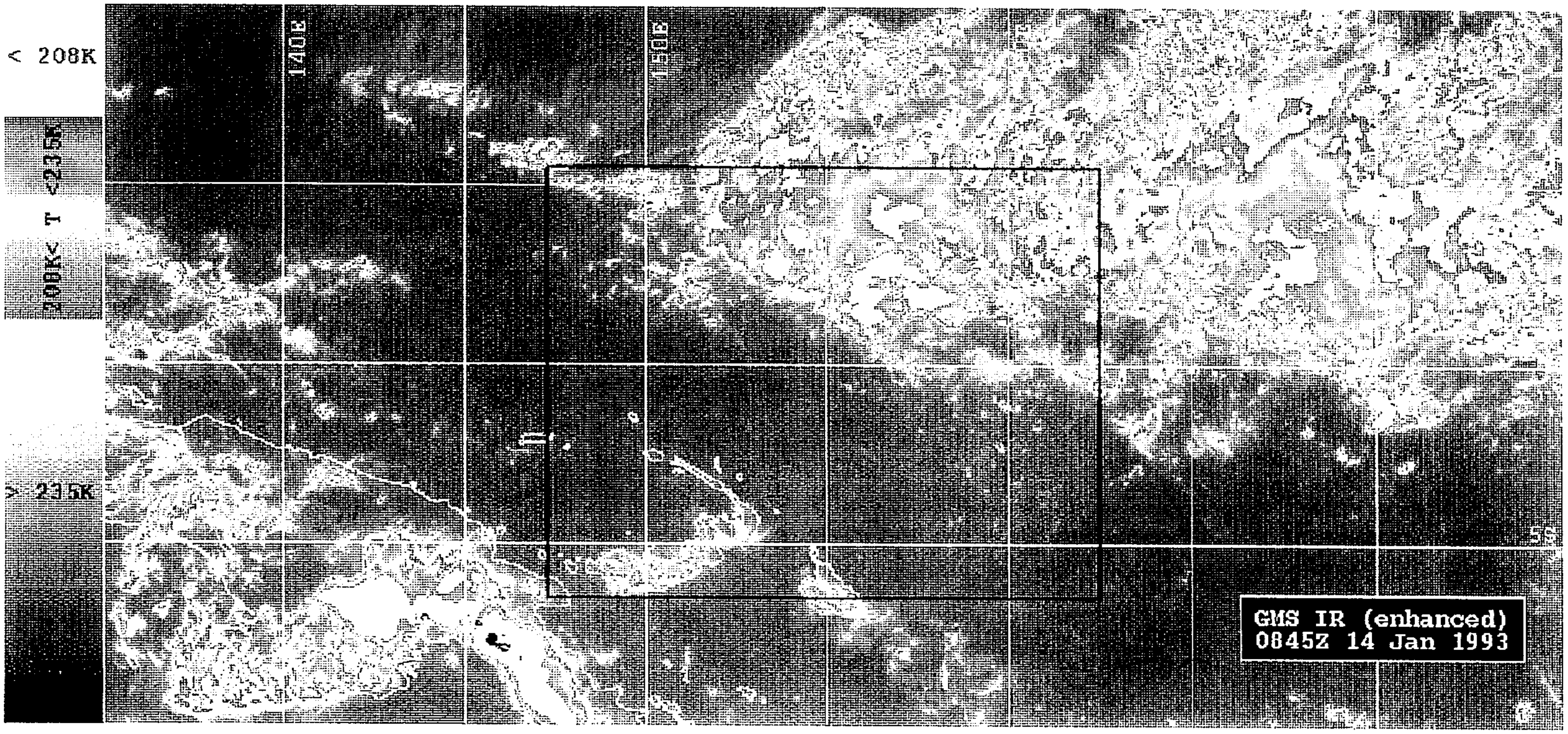

Figure 10. GMS IR image for 0845 UTC 14 January 1993.

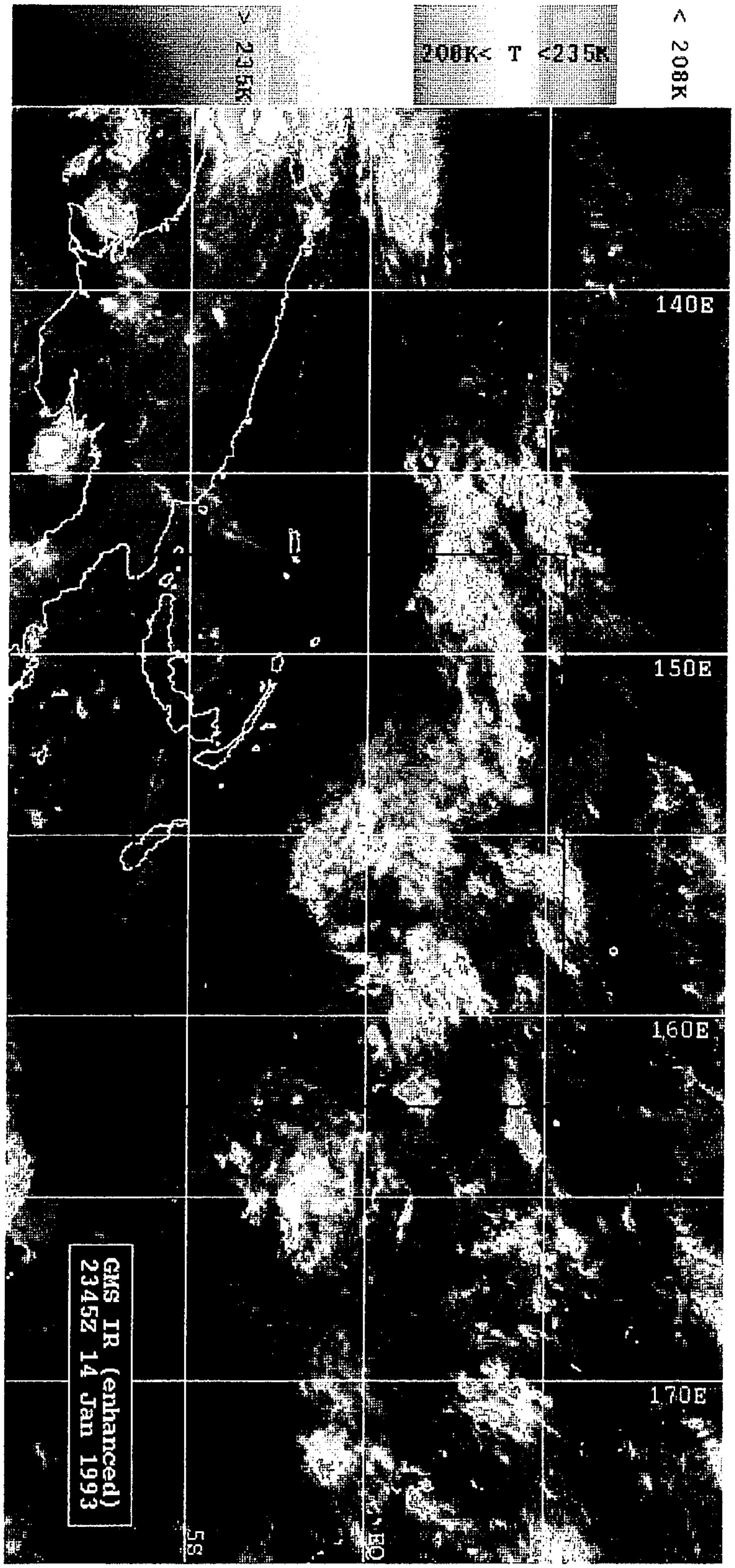

Figure 11. GMS IR image for 2345 UTC 14 January 1993.

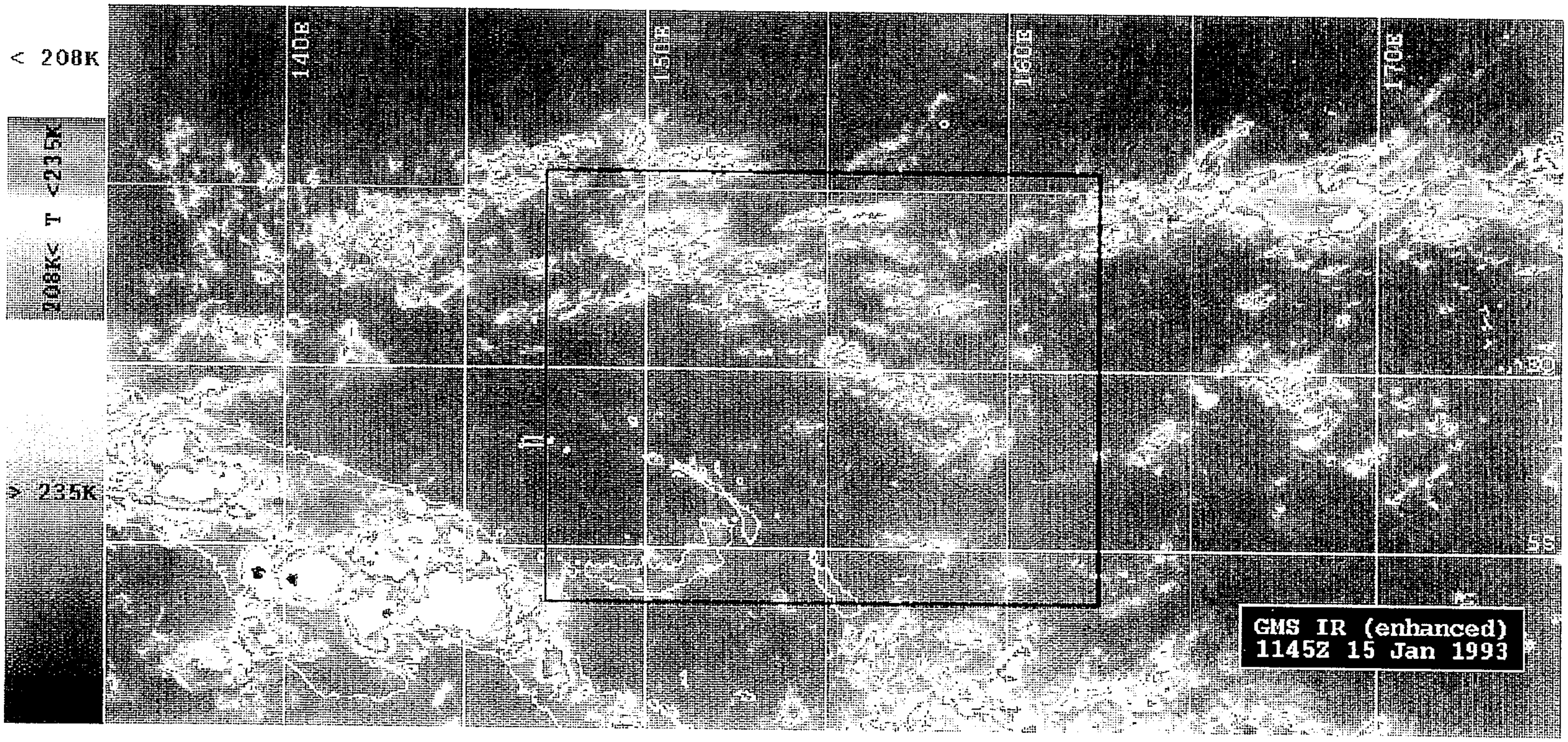

Figure 12. GMS IR image for 1145 UTC 15 January 1993.

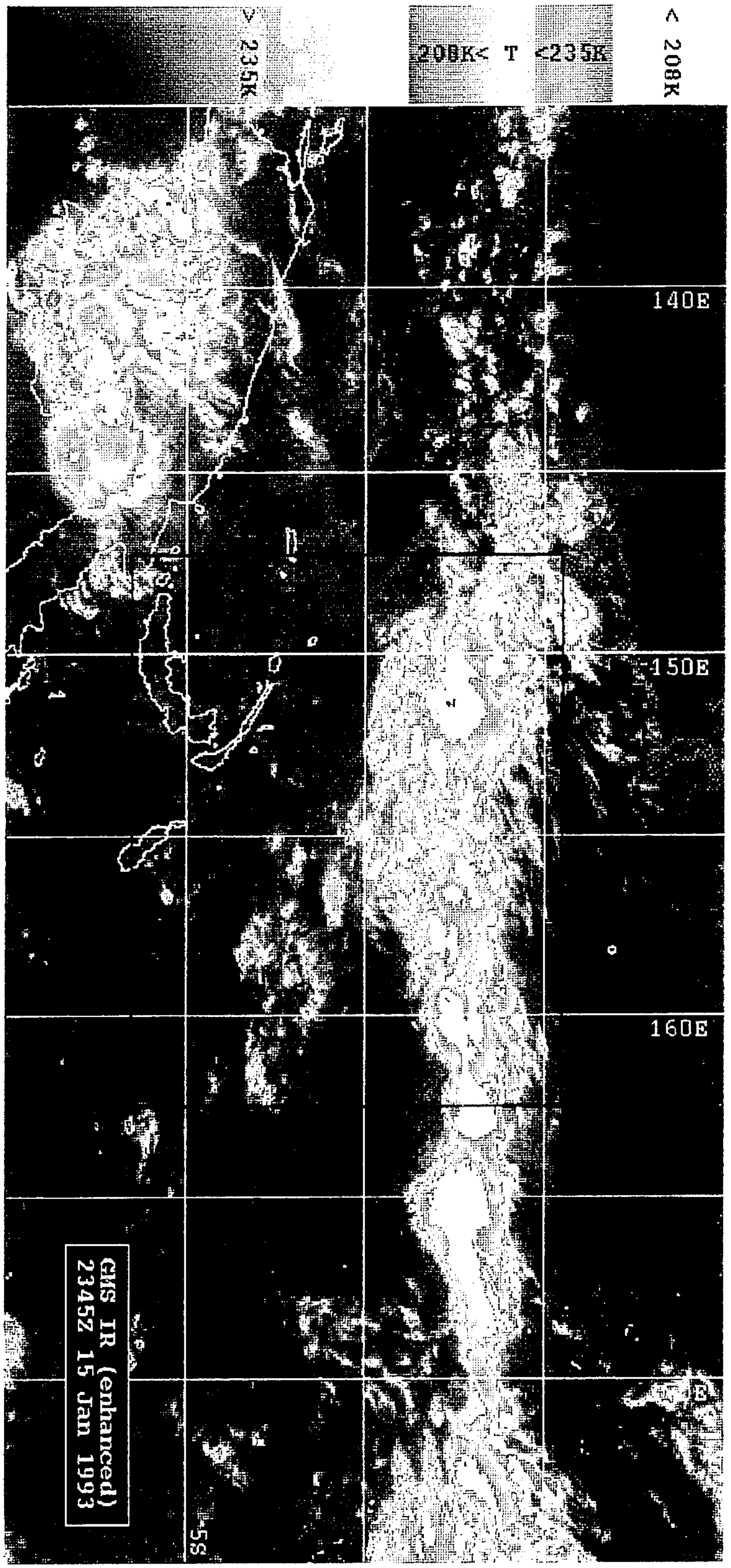

Figure 13. GMS IR image for 2345 UTC 15 January 1993.

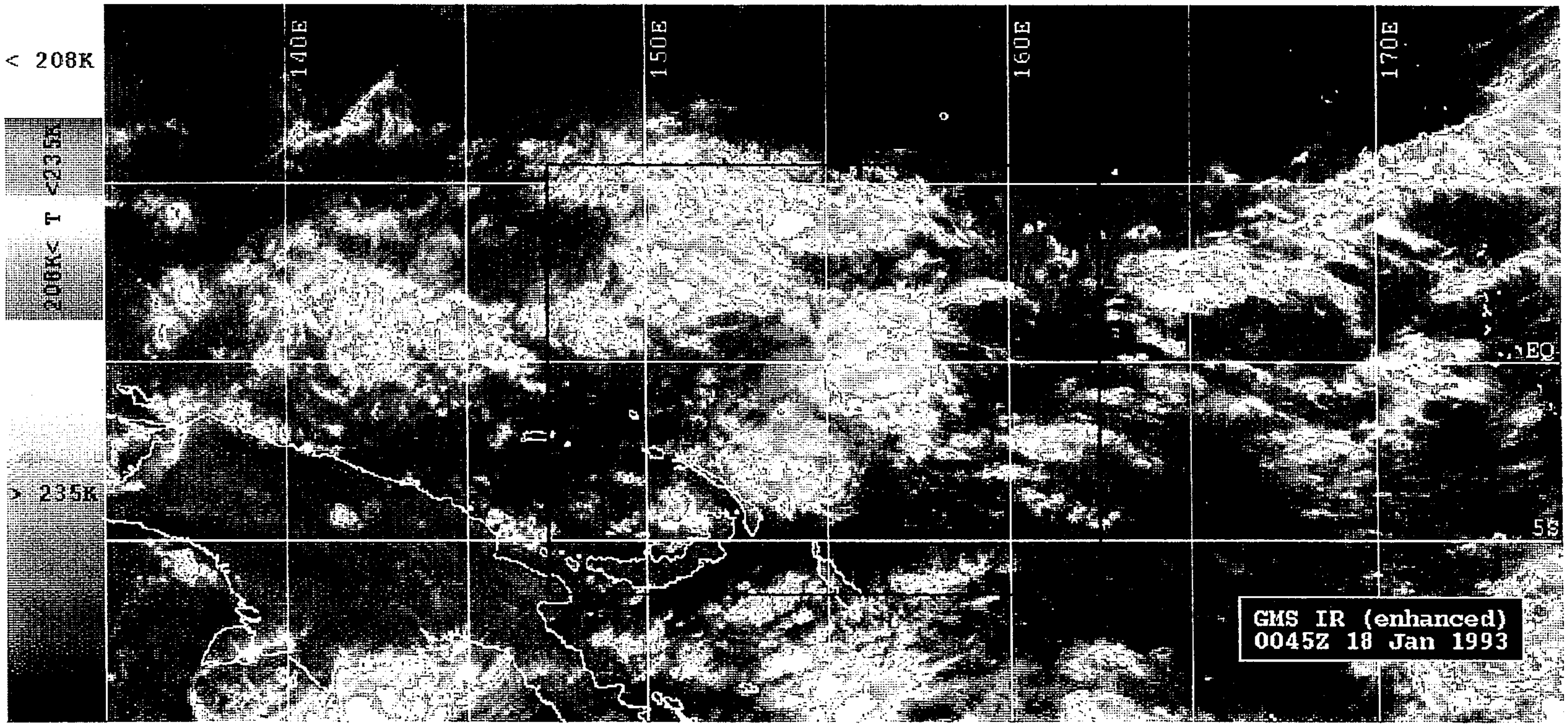

Figure 14. GMS IR image for 0045 UTC 18 January 1993.

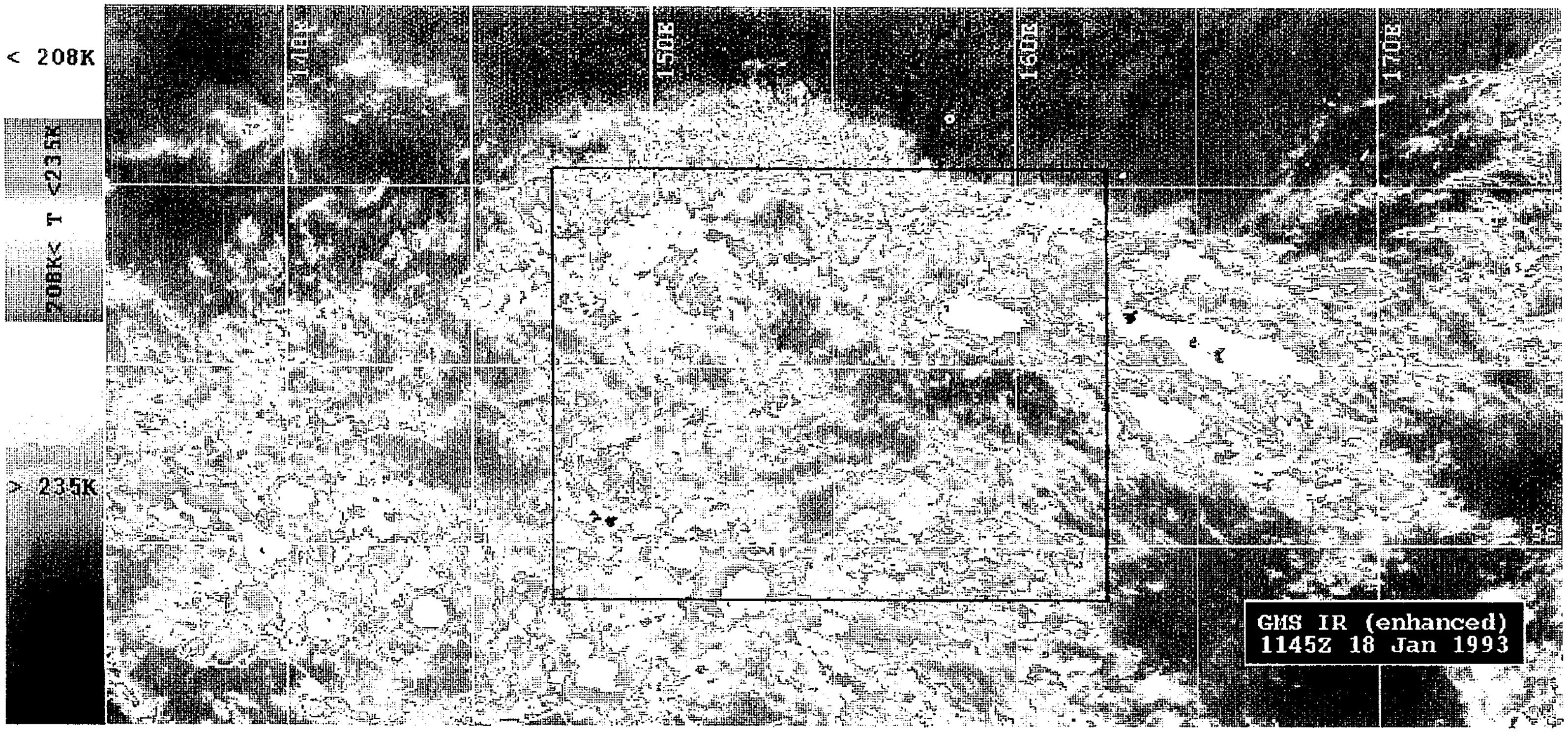

Figure 15. GMS IR image for 1145 UTC 18 January 1993.

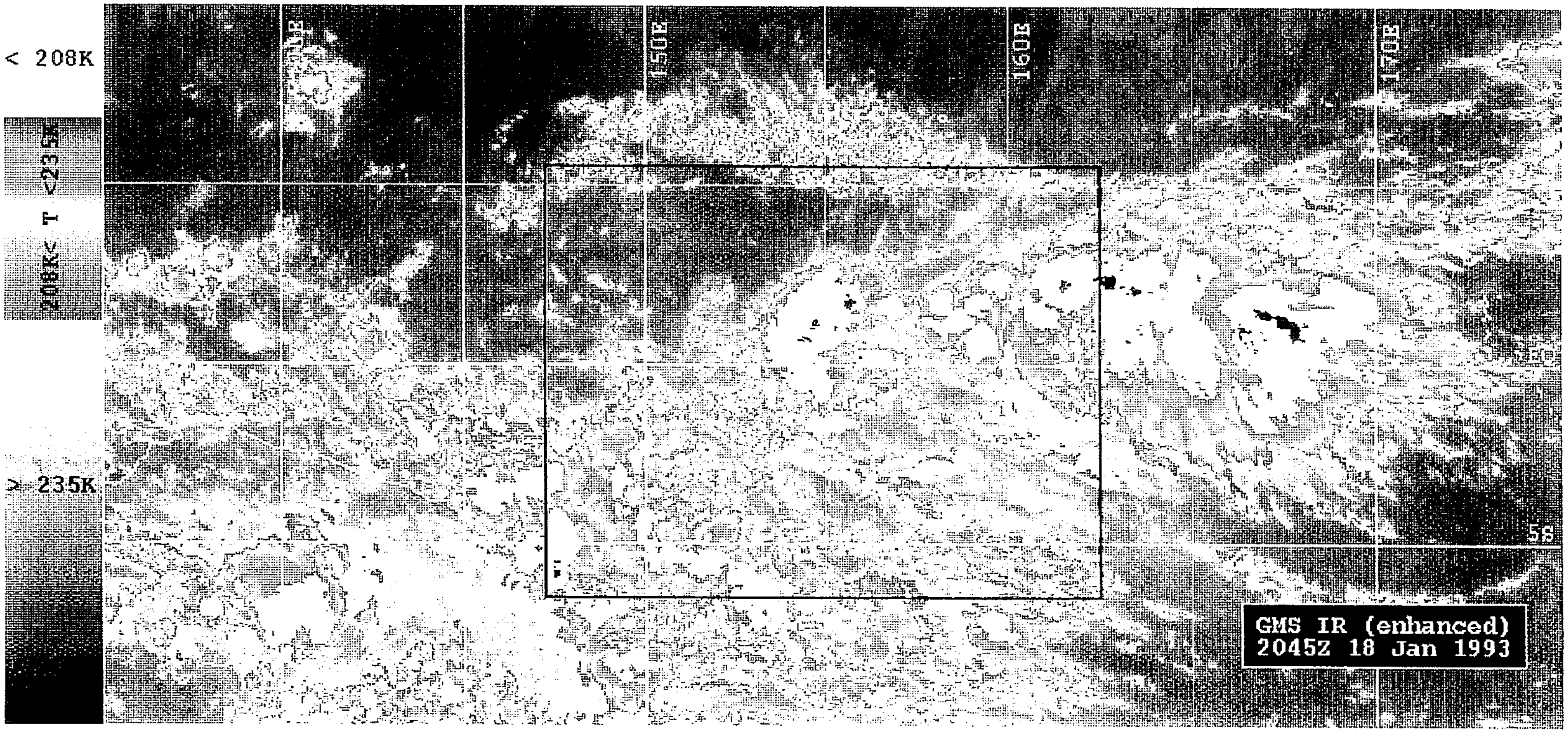

Figure 16. GMS IR image for 2045 UTC 18 January 1993.

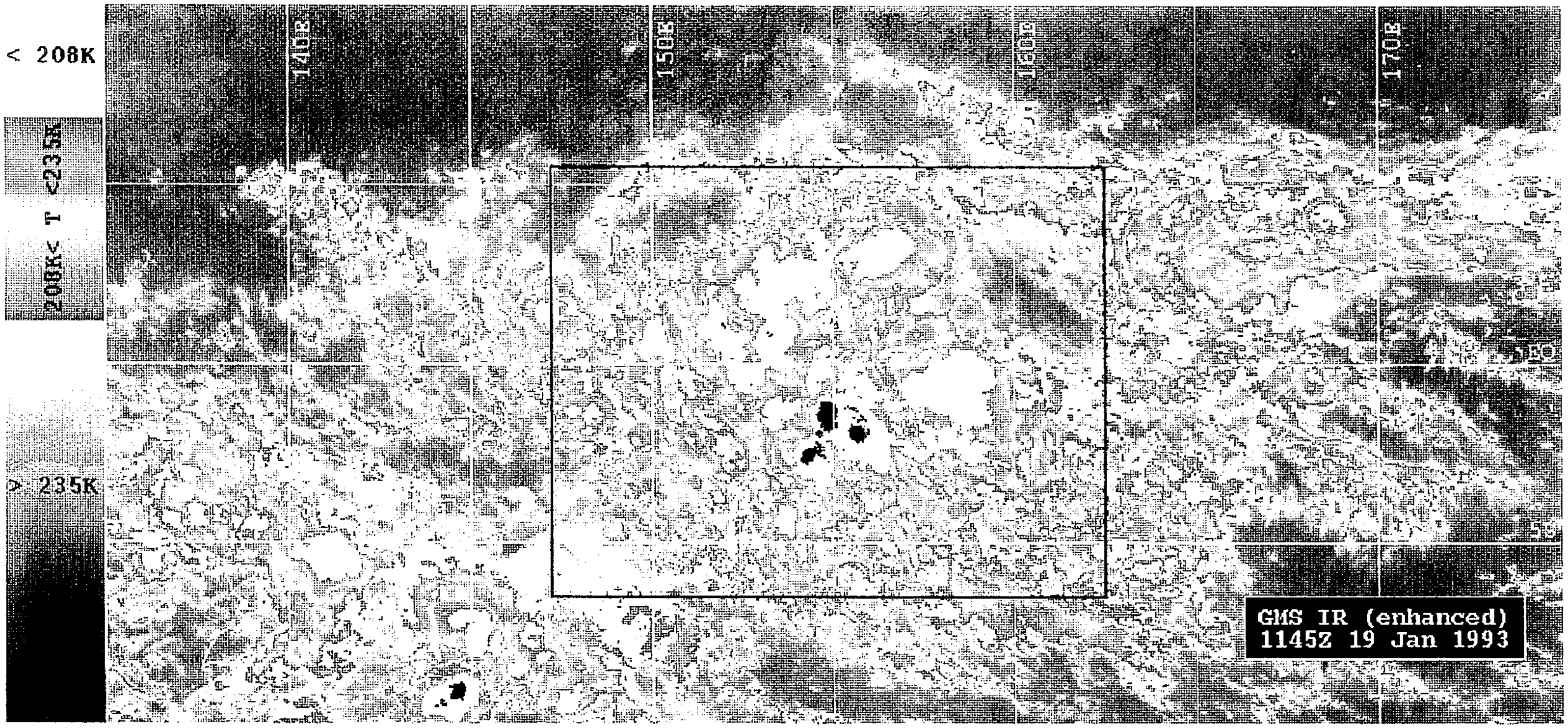

Figure 17. GMS IR image for 1145 UTC 19 January 1993.

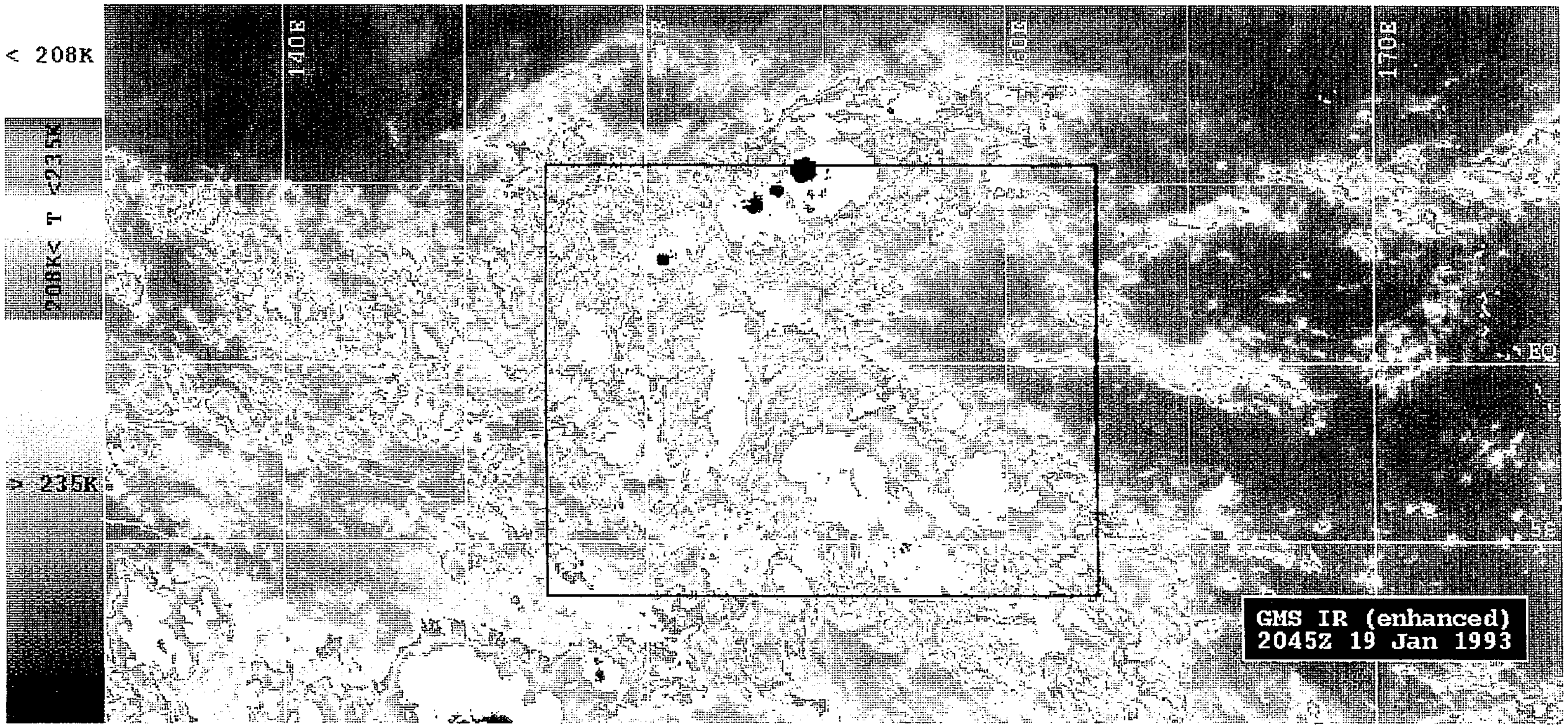

Figure 18. GMS IR image for 2045 UTC 19 January 1993.

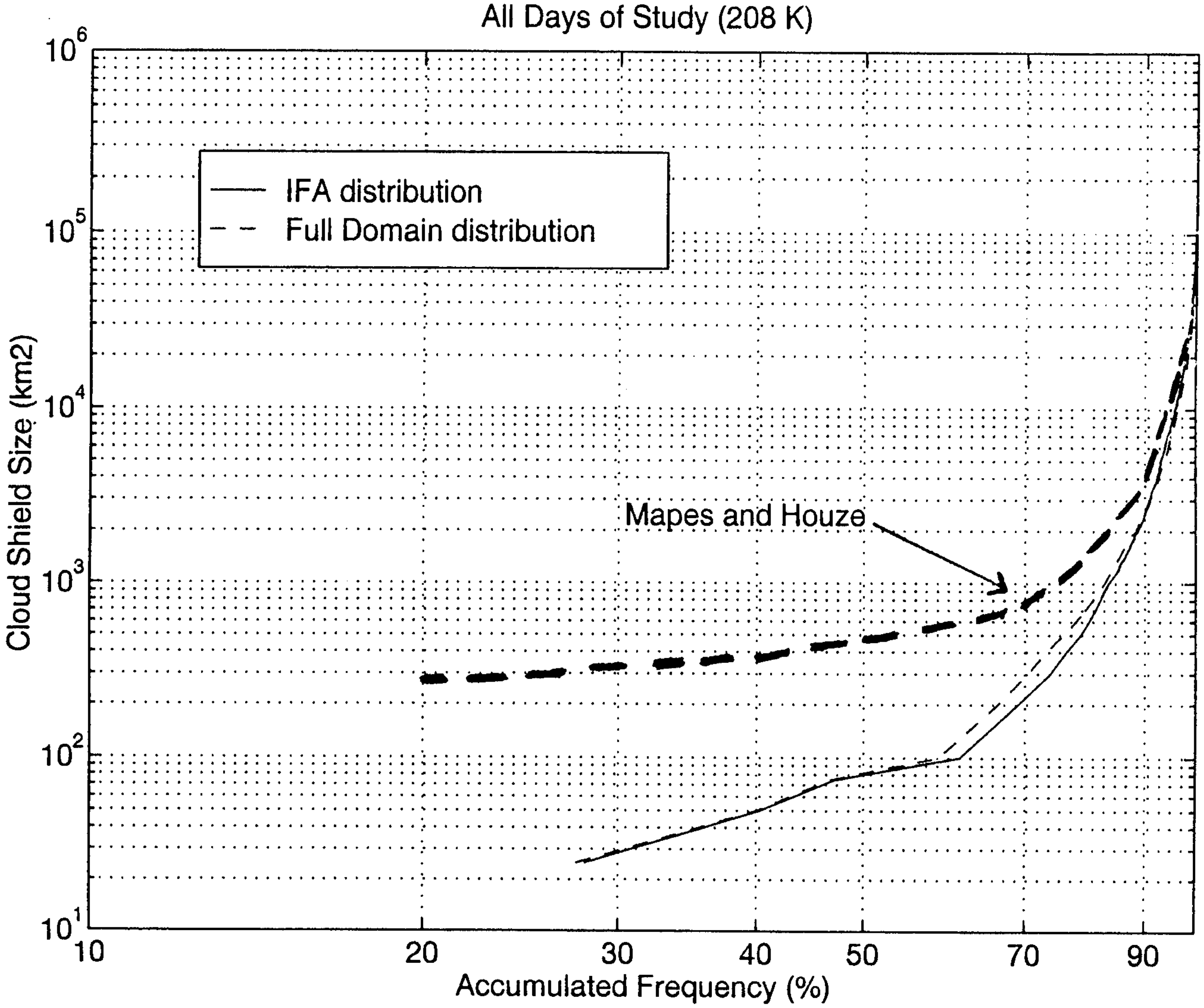

Figure 19. Lognormal test for cloud-cluster size distributions of both the IFA domain and full domain (LSA). Accumulated frequency versus cloud cluster size. The Mapes and Houze (1993) climatological study is shown as a heavy dashed line.

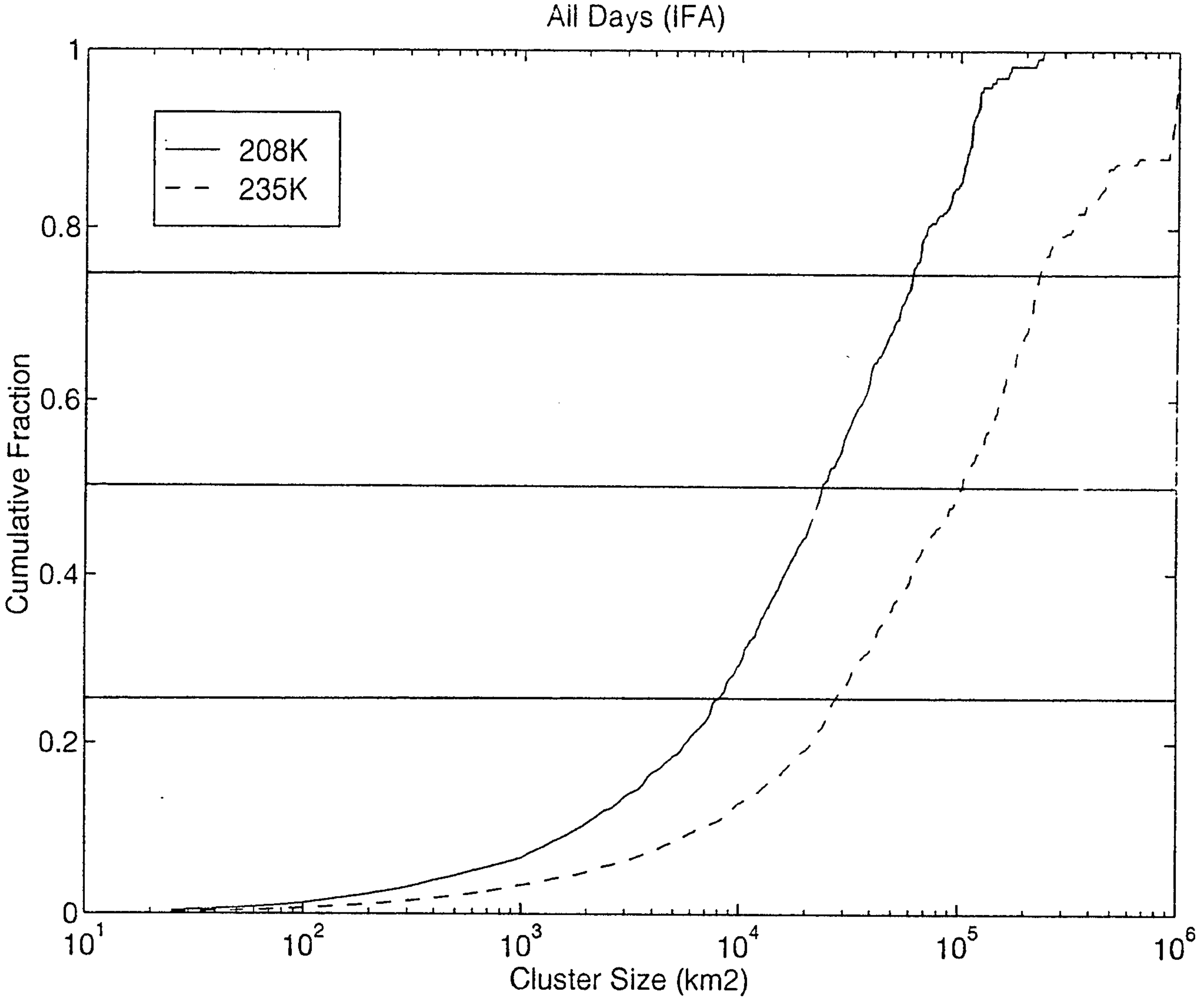

Figure 20. Fraction of the total sampled cloud area that is accounted for by cloud clusters up to the indicated size. The solid horizontal lines divide the size distribution into size quartiles, each contributing an equal amount to the total area of cloud top colder than the indicated temperature threshold.

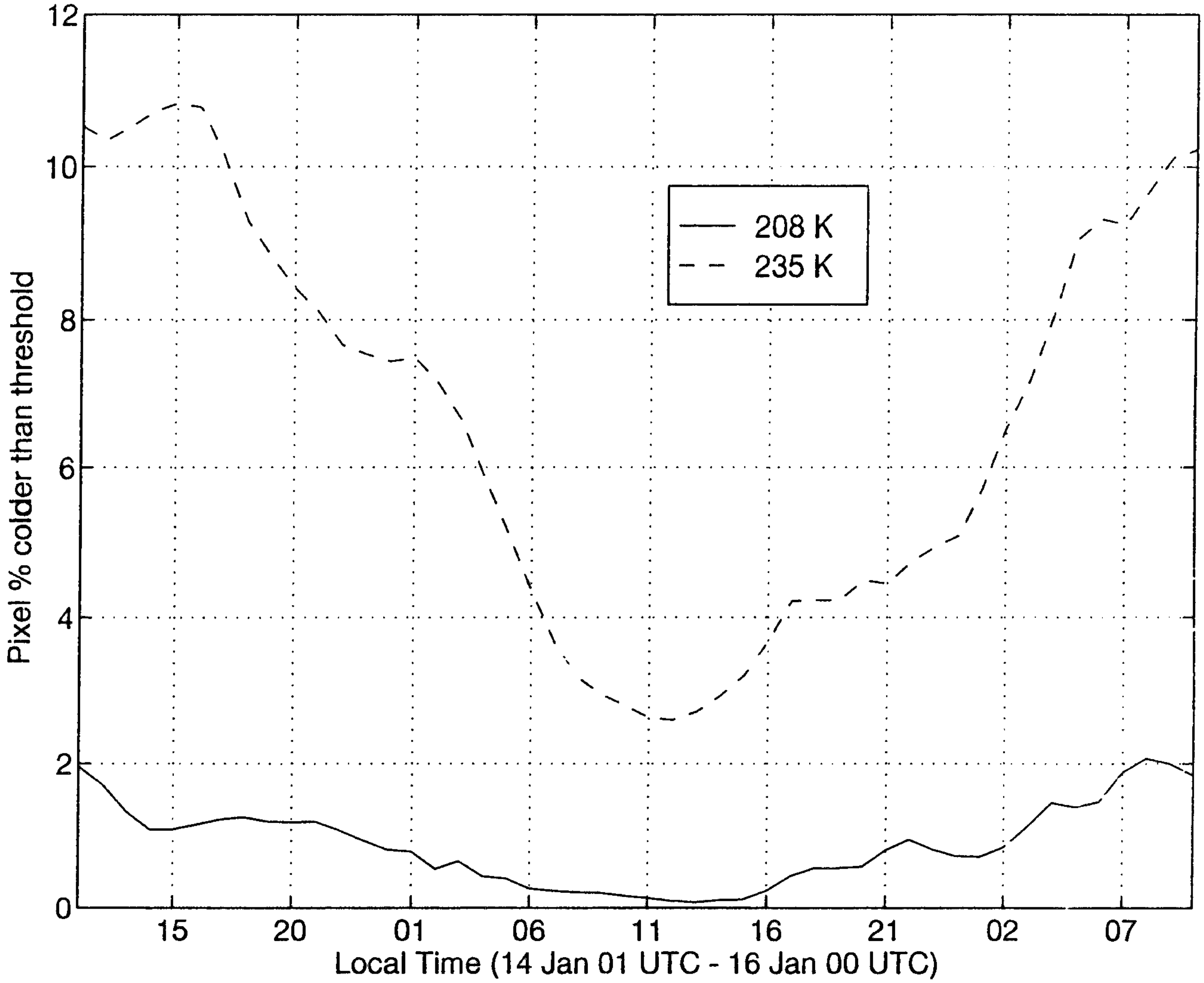

Figure 21. 14-15 January 1993 time series of pixel percentages with temperature values below the indicated thresholds.

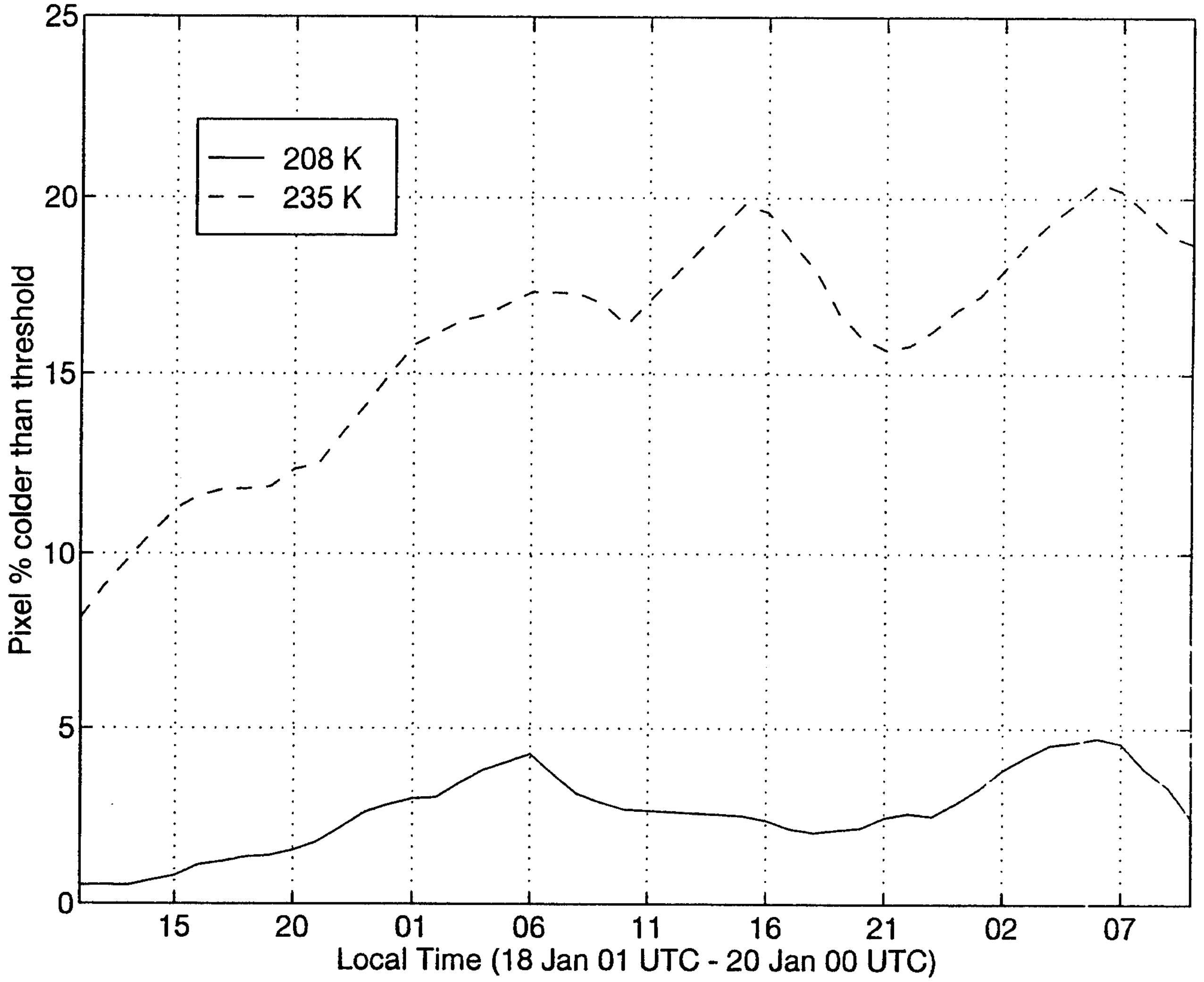

Figure 22. 18-19 January 1993 time series of pixel percentages with temperature values below the indicated thresholds.

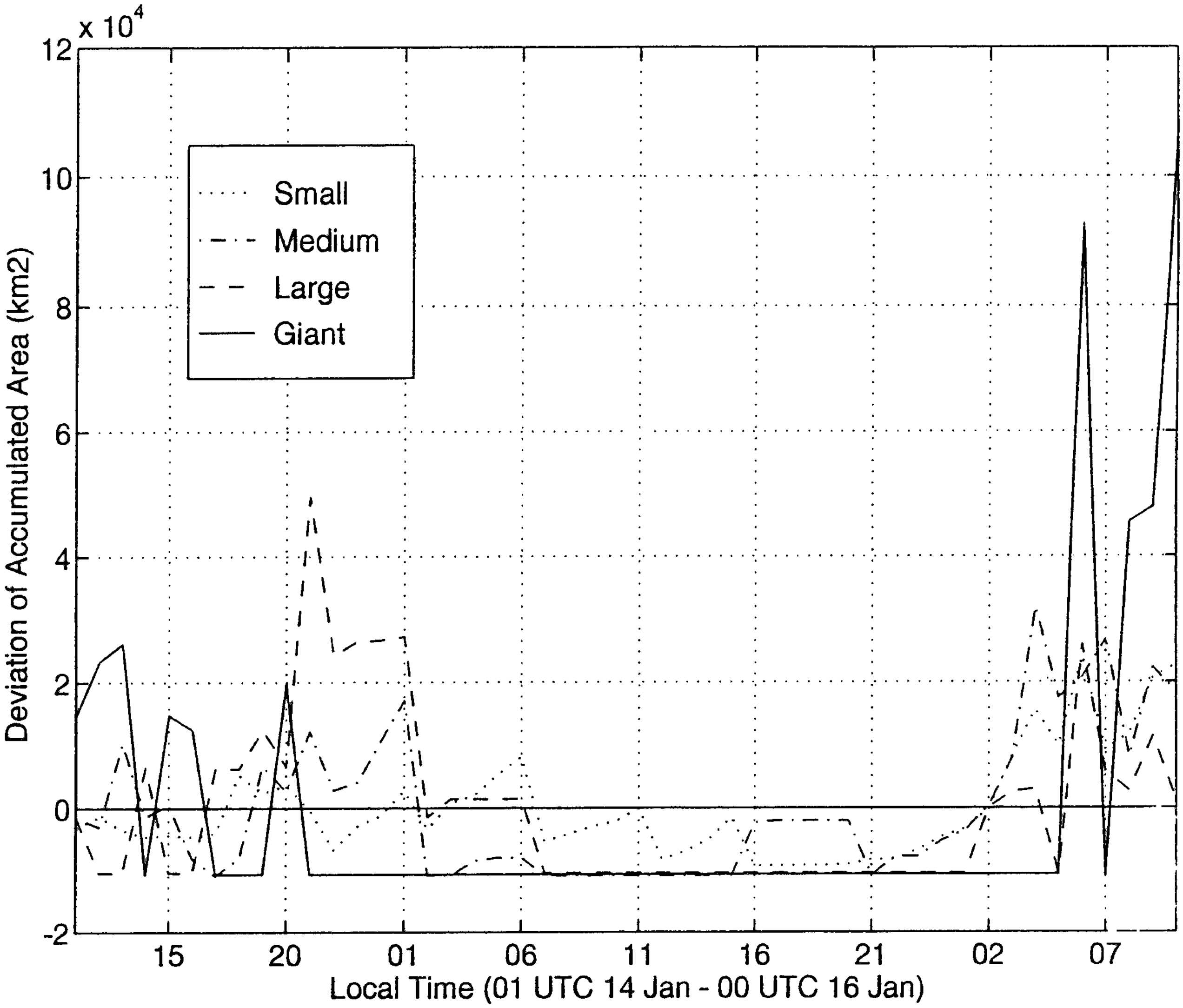

Figure 23. 14-15 January 1993 time series of the deviation from the mean accumulated area of small, medium, large, and giant cloud cluster-sizes using a threshold of 235°K.

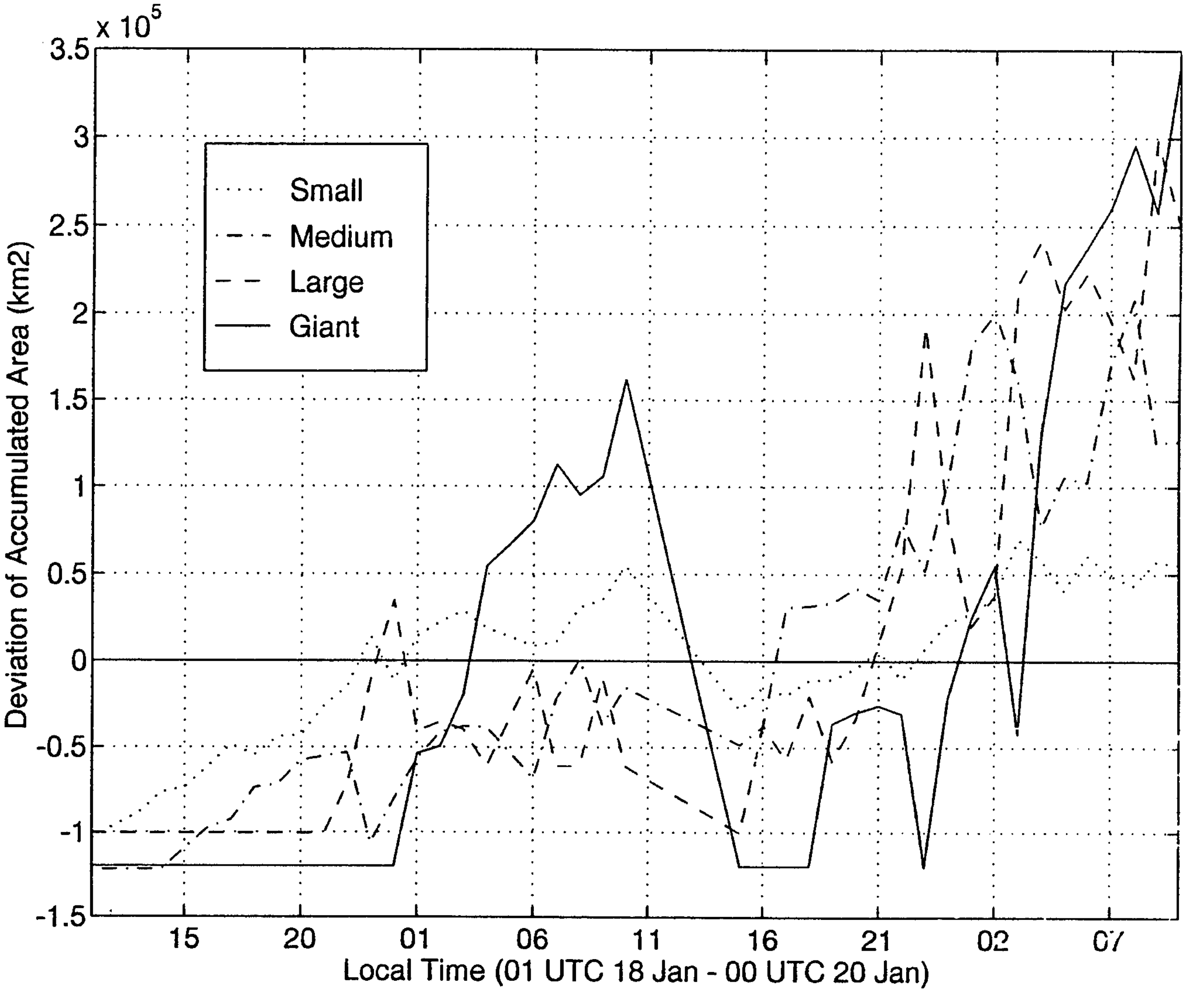

Figure 24. 18-19 January 1993 time series of the deviation from the mean accumulated area of small, medium, large, and giant cloud cluster-sizes using a threshold of 235°K.

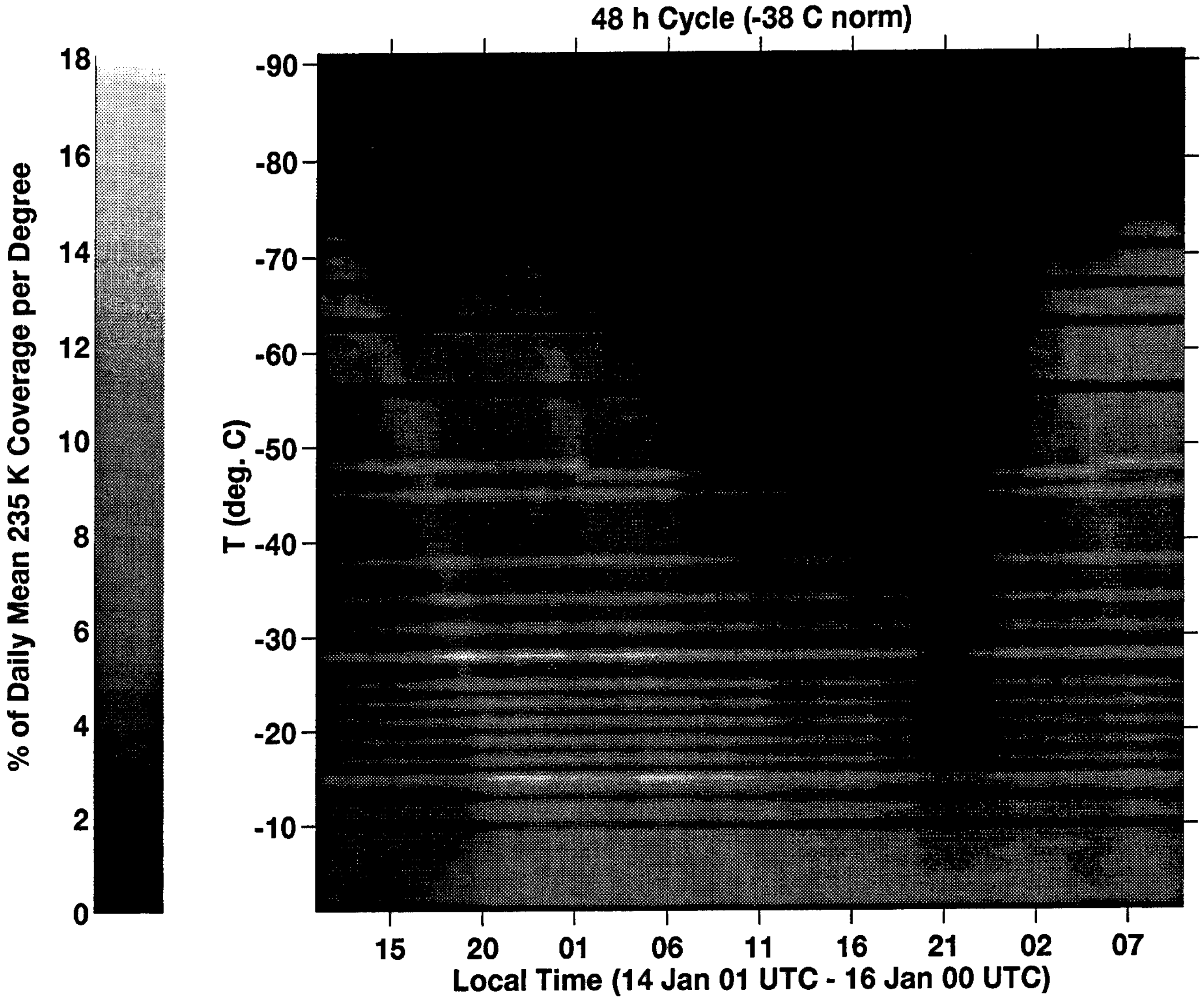

Figure 25. 14-15 January 1993 time series showing percentage of the daily mean moderately cold (< 235°K) cloud area, within 1°C temperature intervals at the indicated temperatures, as a function of time of day, in the IFA domain.

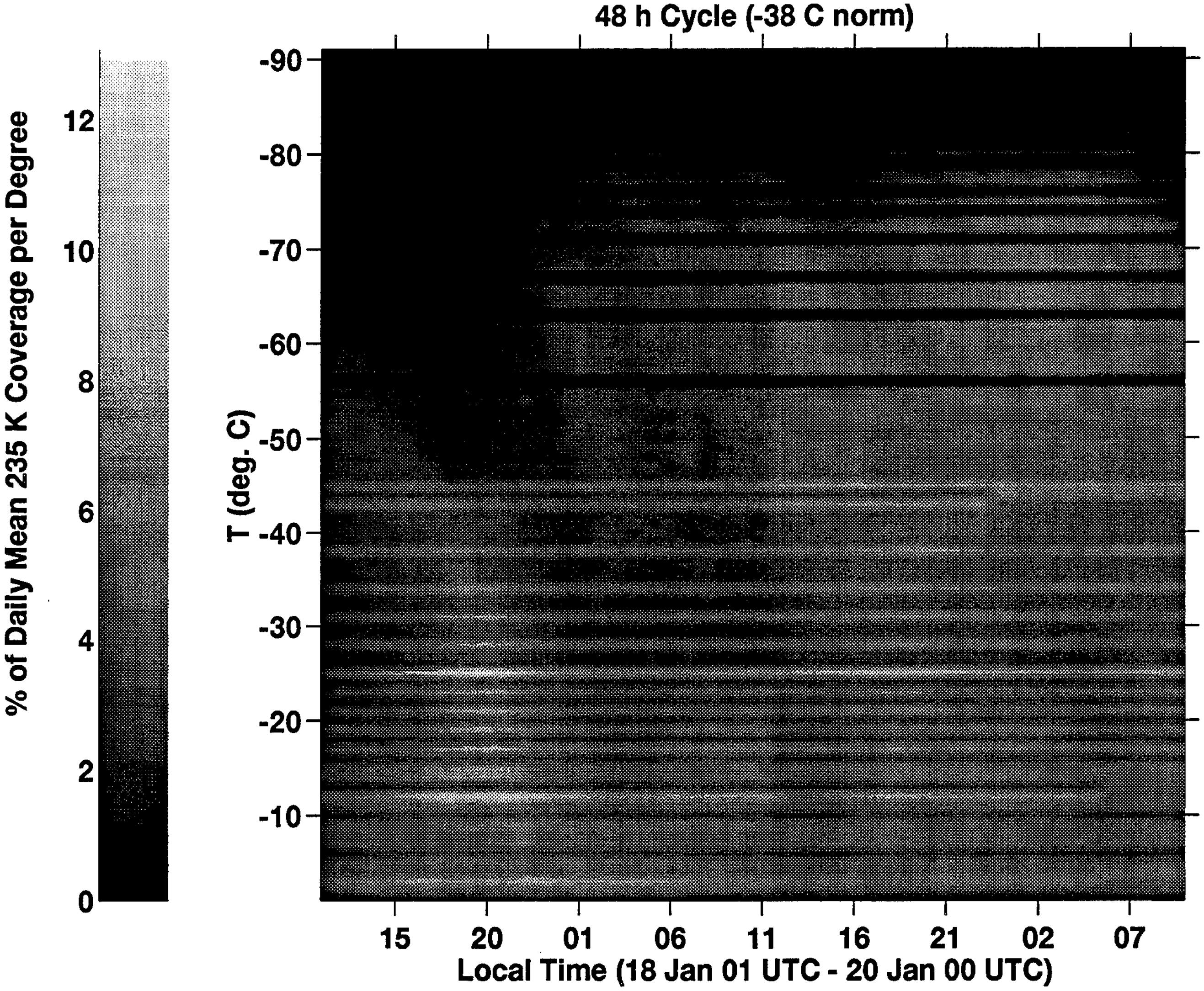

Figure 26. 18-19 January 1993 time series showing percentage of the daily mean moderately cold (< 235°K) cloud area, within 1°C temperature intervals at the indicated temperatures, as a function of time of day, in the IFA domain.

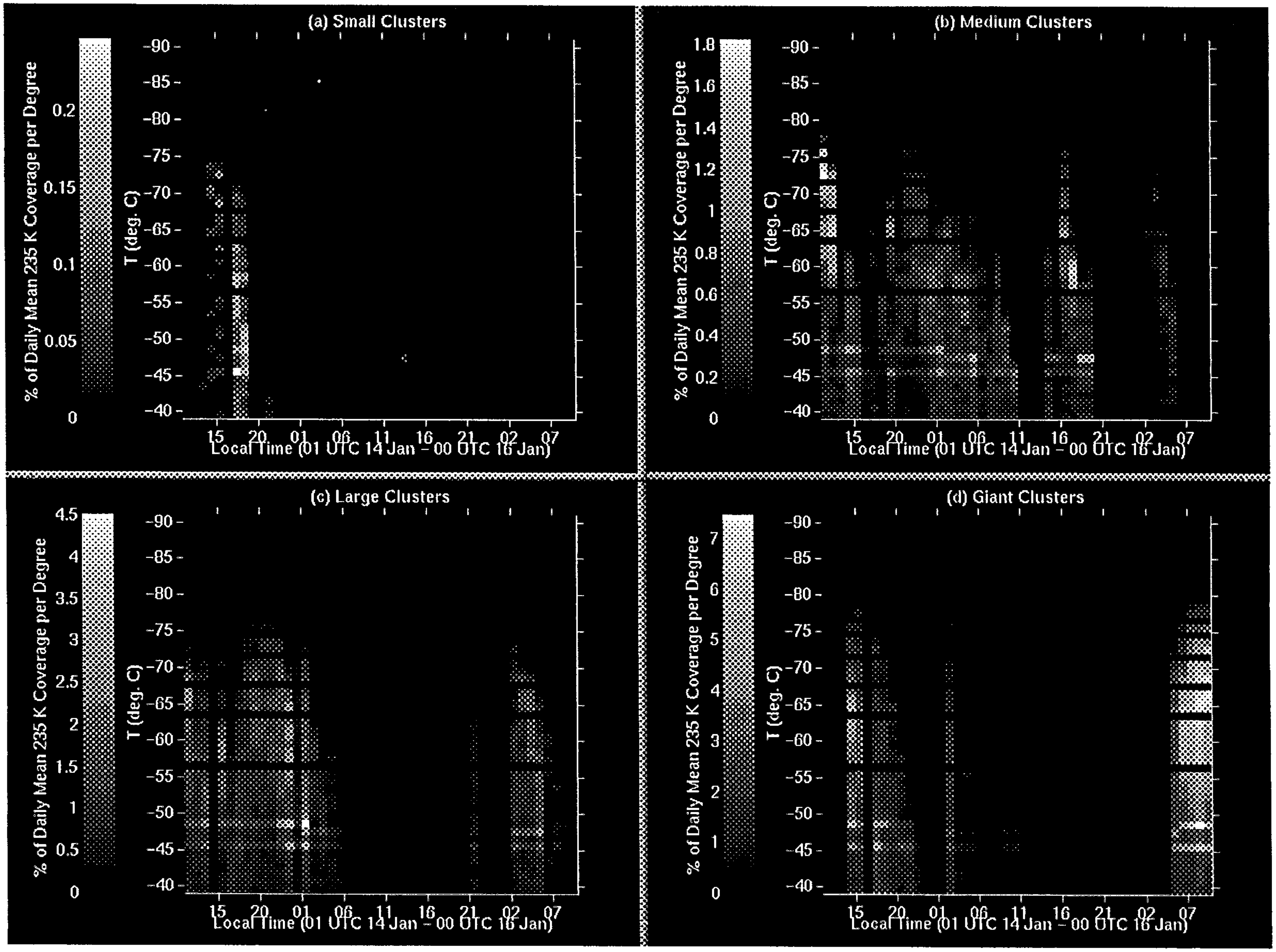

Figure 27. 14-15 January 1993 time series subdivided into moderately cold (<235°K) cloud-cluster quartiles: (a) small, (b) medium, (c) large, (d) giant. The vertical scale differs from Figure 25 because only temperatures colder than 235°K lie within the 235°K cloud clusters.

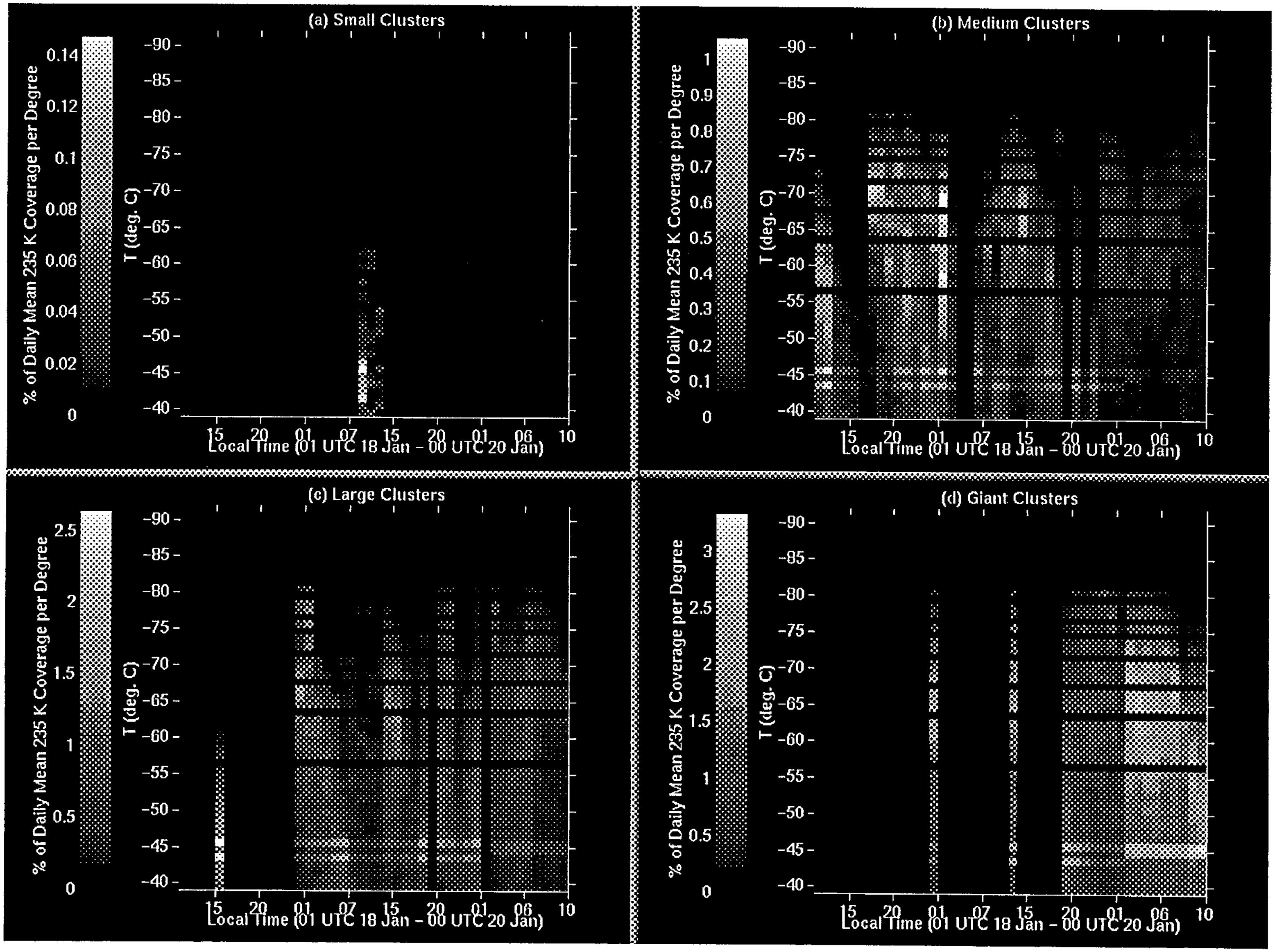

Figure 28. 18-19 January 1993 time series subdivided into moderately cold (<235°K) cloud-cluster quartiles: (a) small, (b) medium, (c) large, (d) giant.

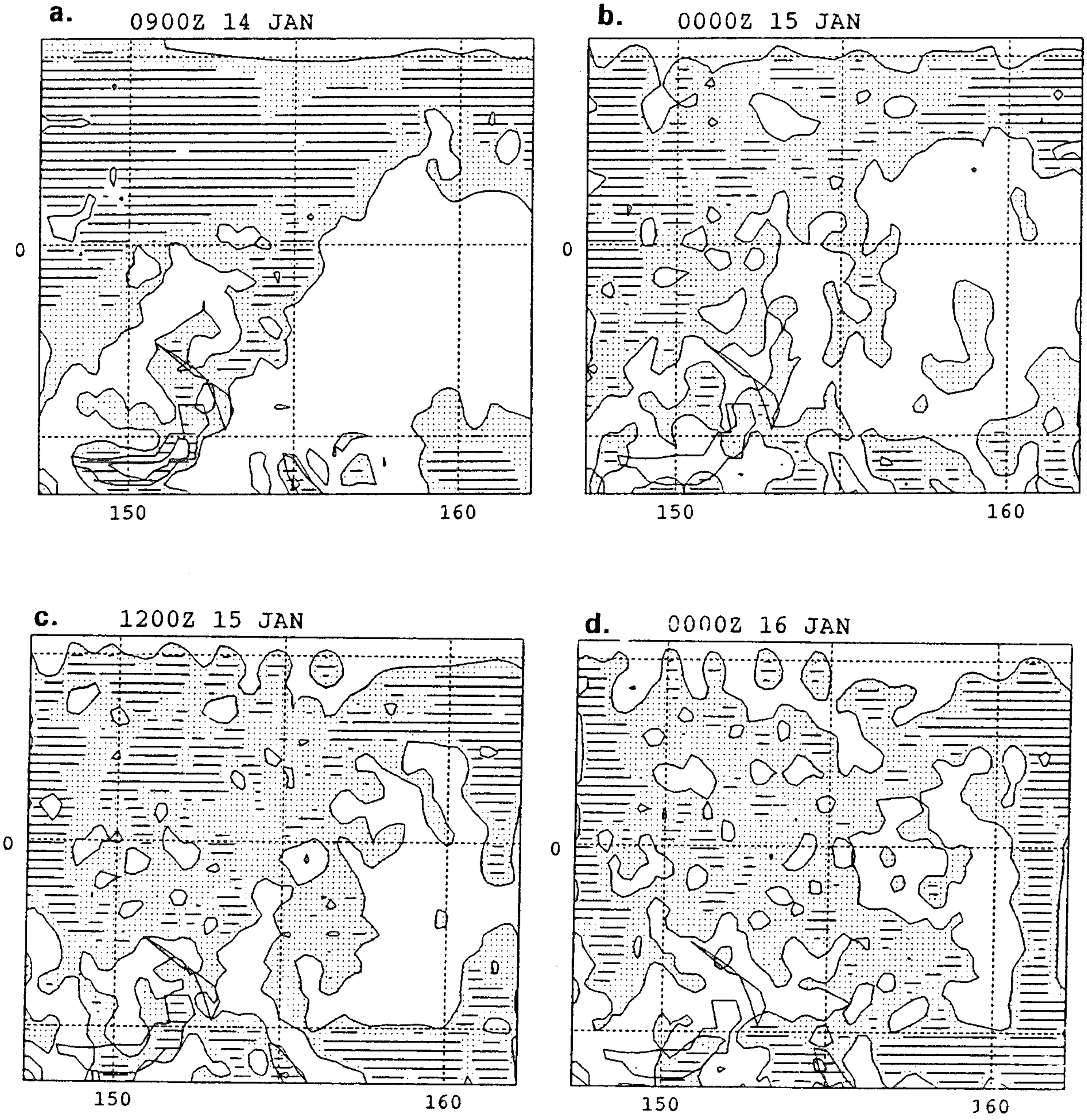

Figure 29. Model forecasts for 14-15 January 1993 of total cloud cover in the IFA domain for (a) 9-h, (b) 24-h, (c) 36-h, and (d) 48-h model integration times.

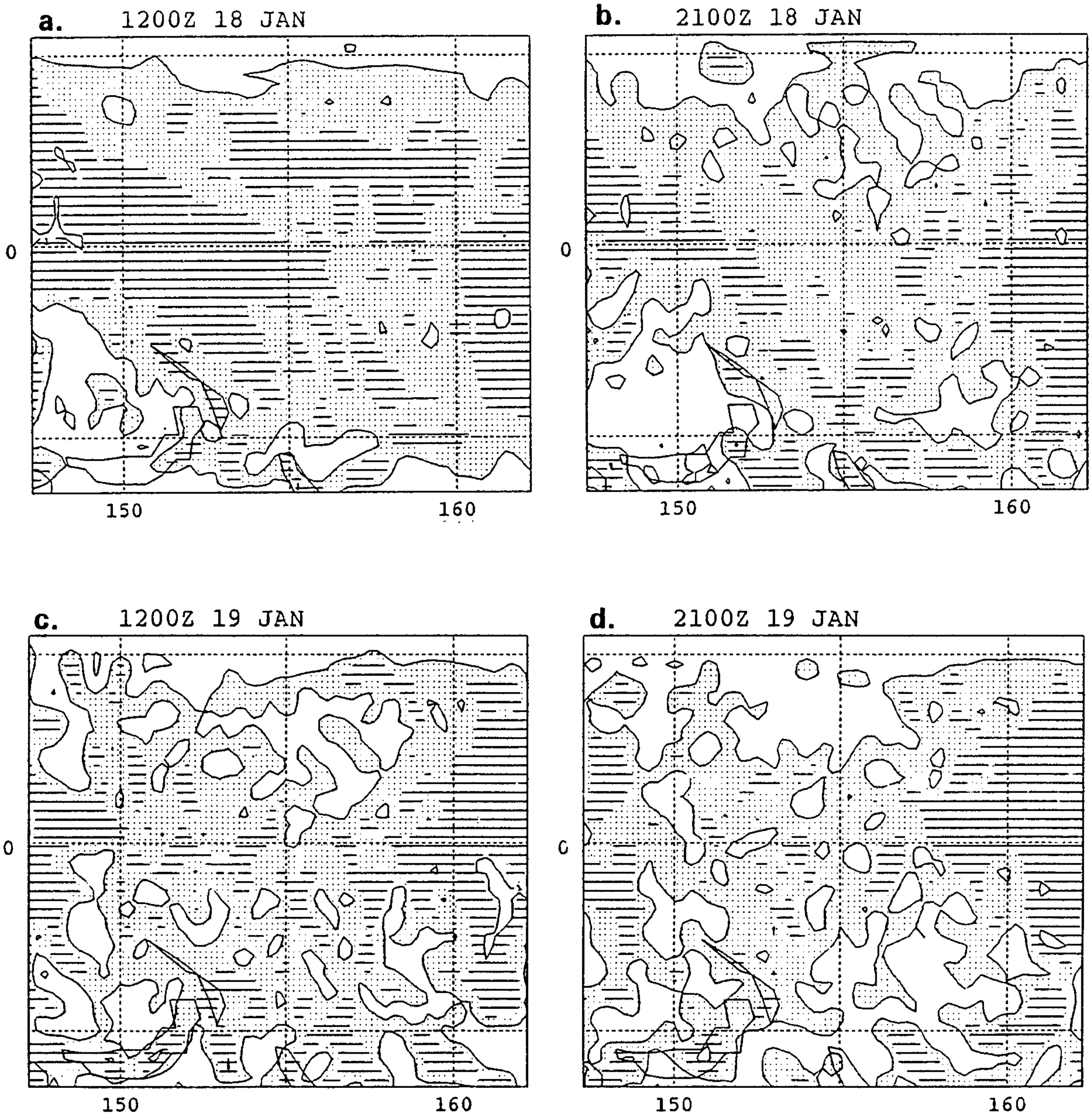

Figure 30. Model forecasts for 18-19 January 1993 of total cloud cover in the IFA domain for (a) 12-h, (b) 21-h, (c) 36-h, and (d) 45-h model integration times.

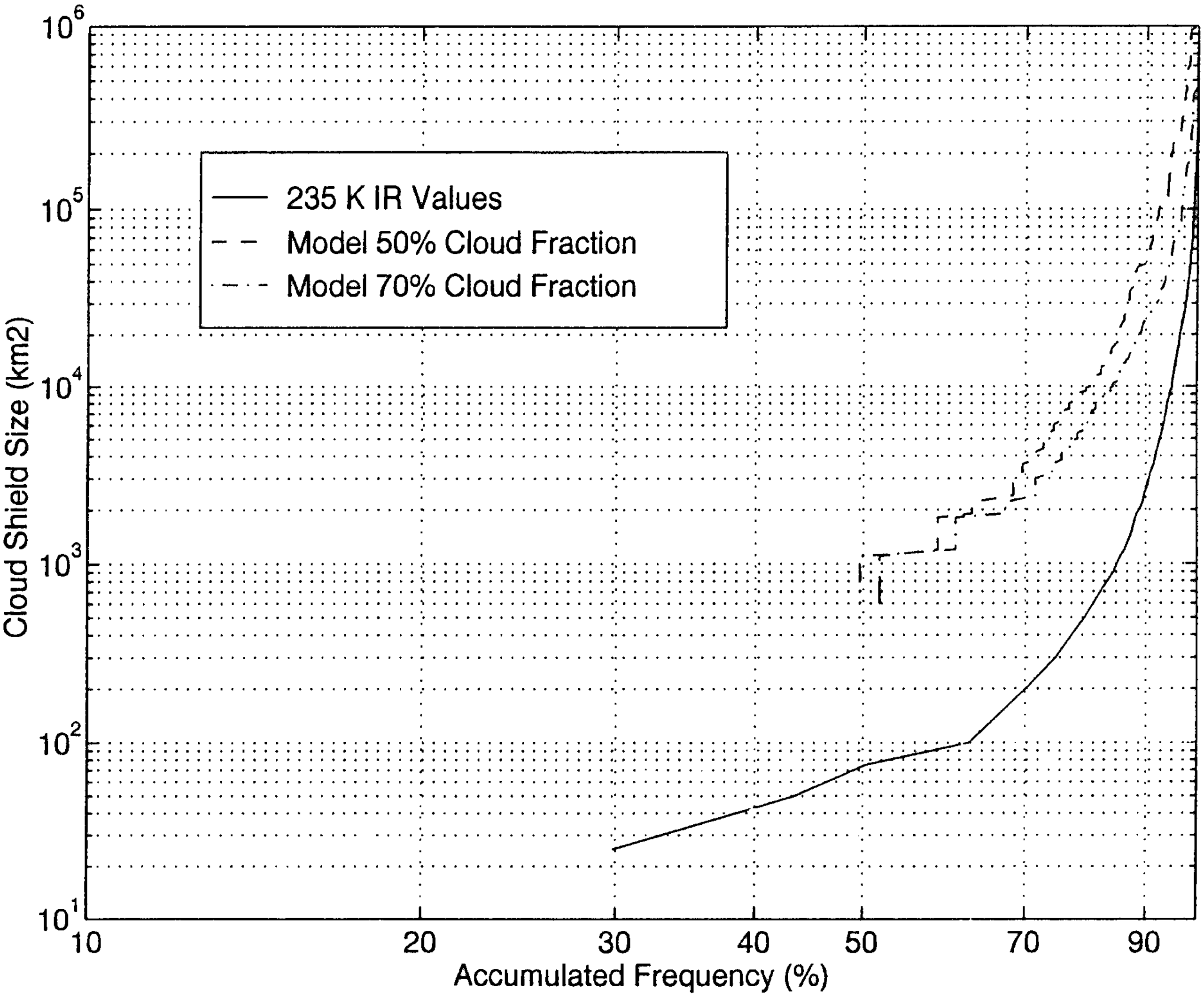

Figure 31. Lognormal test for model cloud-cluster size distributions of the IFA domain for 50% and 70% model cloud fraction showing accumulated frequency versus cloud cluster size. The 235°K IR distribution is shown as a solid line.

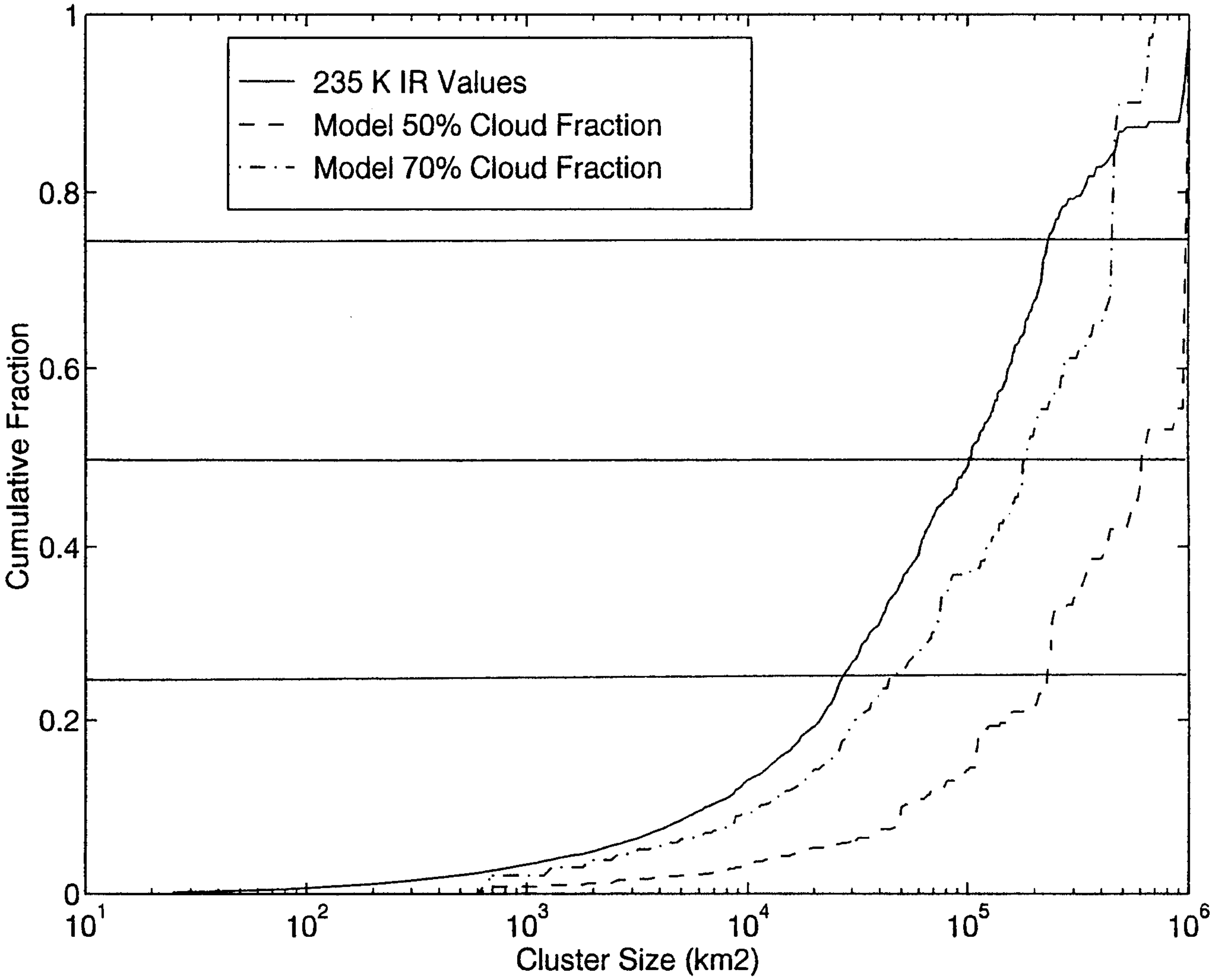

Figure 32. Fraction of the model's total cloud area that is accounted for by cloud clusters up to the indicated size. The solid horizontal lines divide the size distribution into size quartiles, each contributing an equal amount to the total area of cloud defined by the indicated model cloud fraction threshold. The 235°K IR distribution is shown as a solid line.

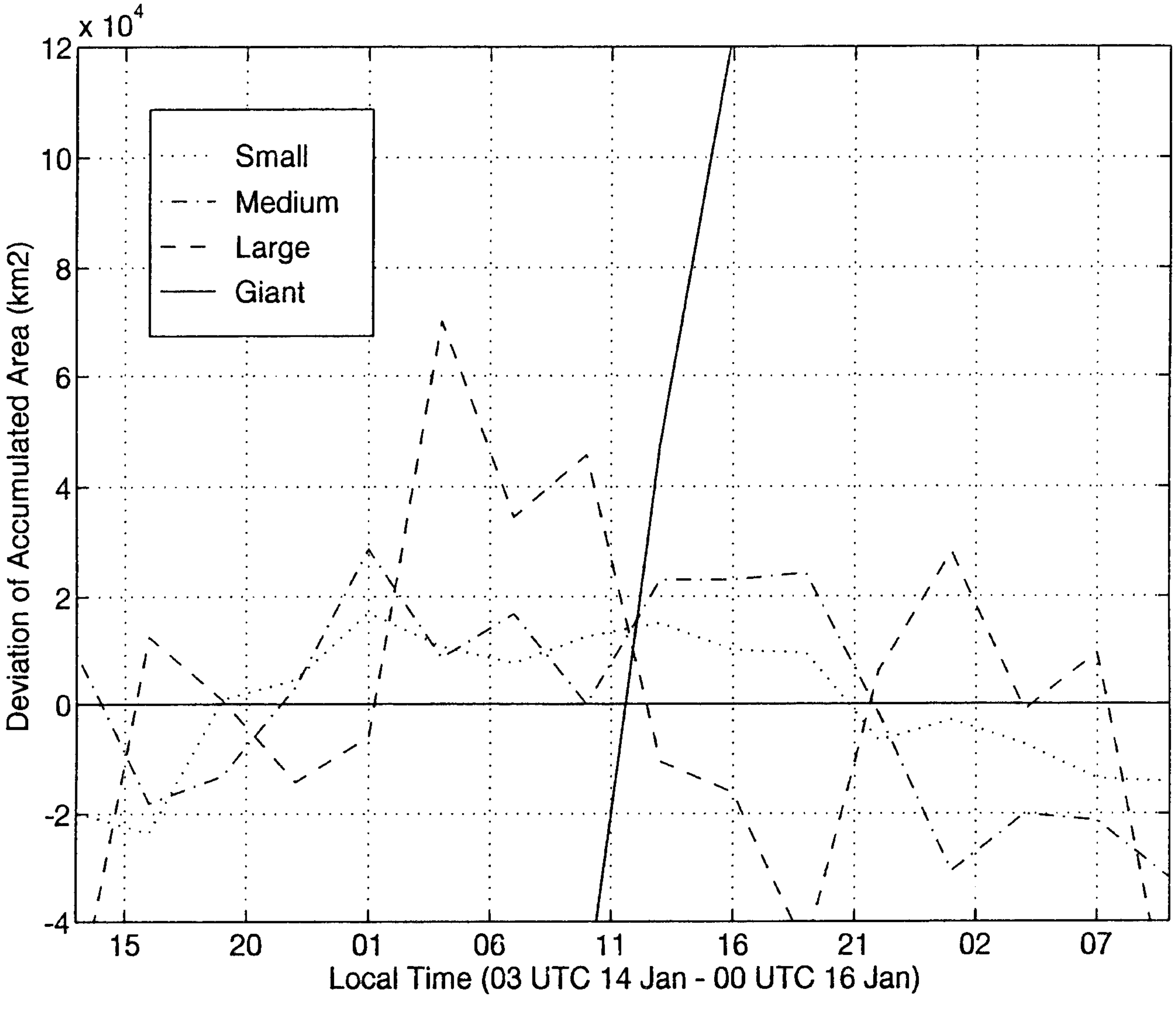

Figure 33. 14-15 January 1993 time series of the deviation from the mean accumulated area of small, medium, large, and giant cloud cluster-sizes using 70% model cloud fraction as a threshold.

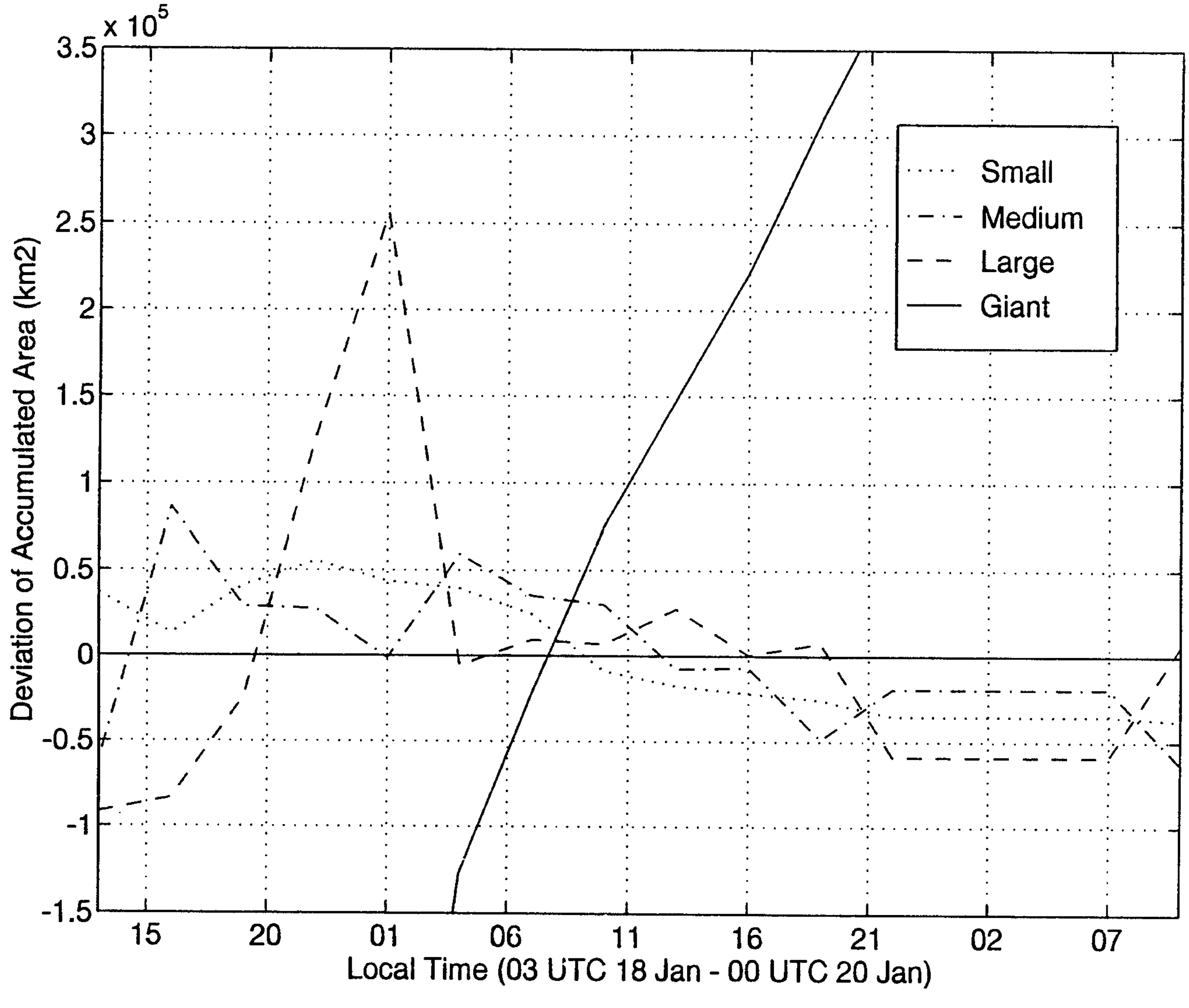

Figure 34. 18-19 January 1993 time series of the deviation from the mean accumulated area of small, medium, large, and giant cloud cluster-sizes using 70% model cloud fraction as a threshold.

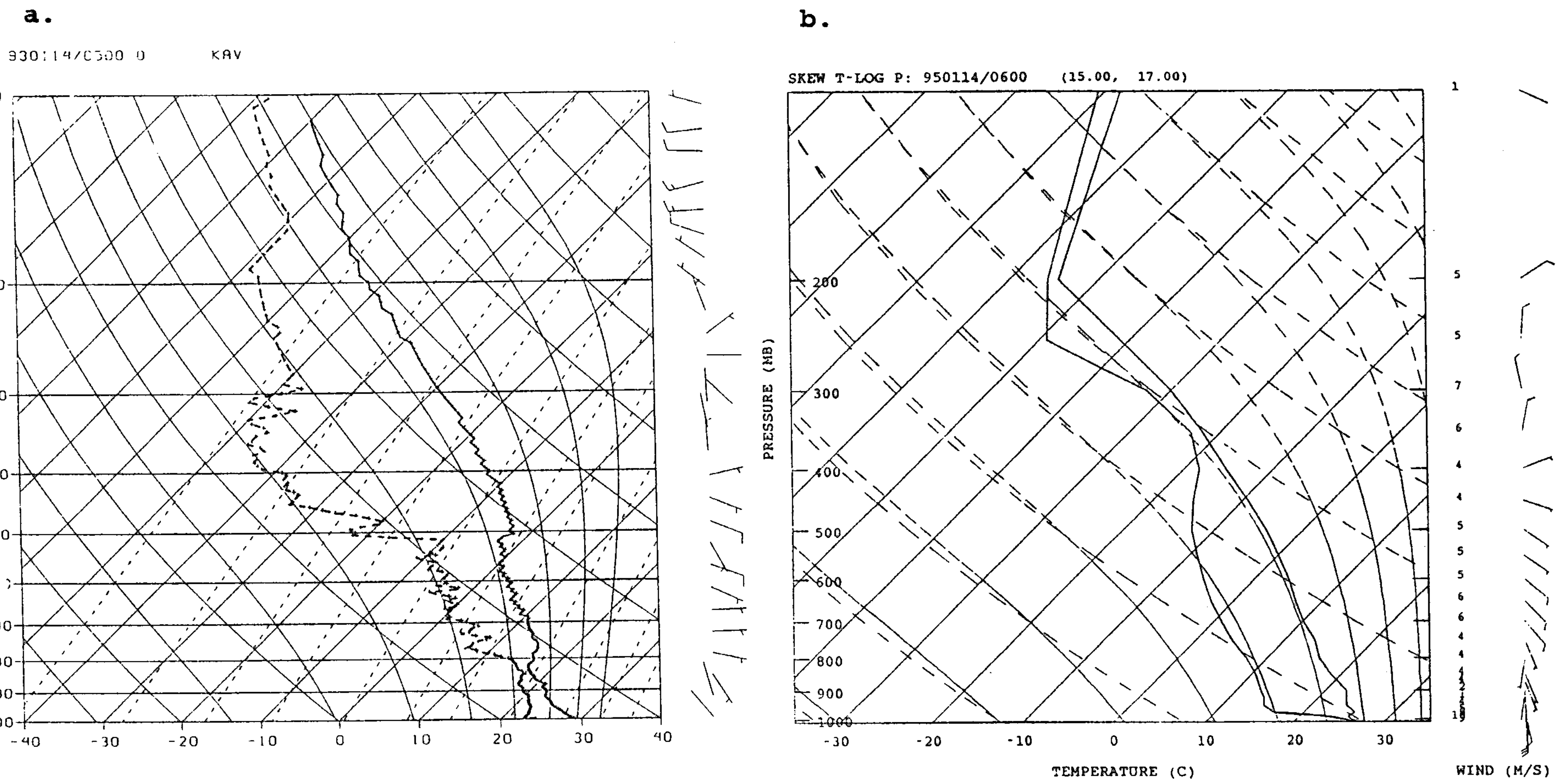

Figure 35. (a) Kavieng environmental sounding of 05 UTC 14 January 1993, (b) 6-h model forecast sounding of 06 UTC 14 January 1993.

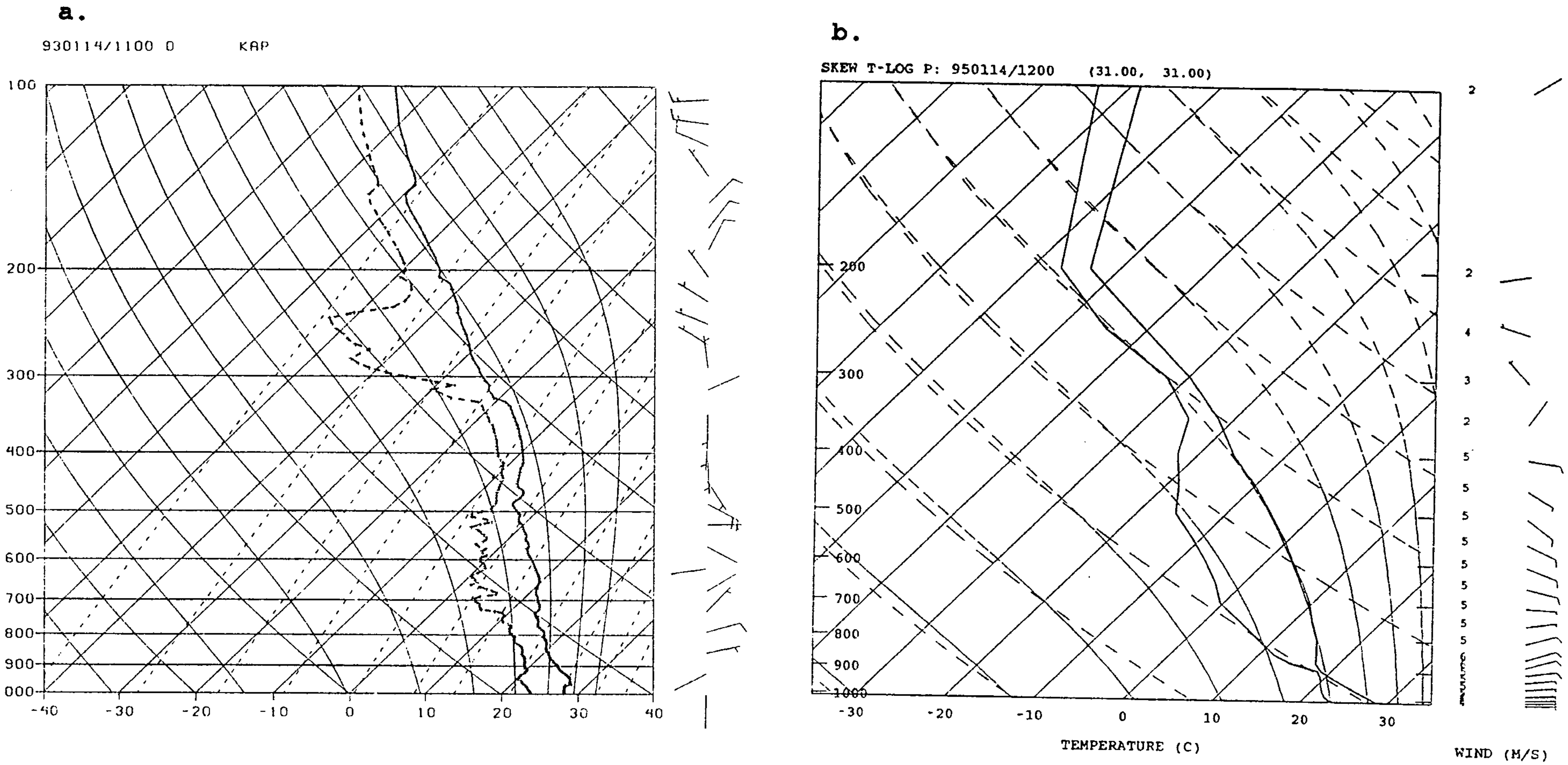

Figure 36. (a) Kapingamaranji environmental sounding of 11 UTC 14 January 1993, (b) 12-h model forecast sounding of 12 UTC 14 January 1993.

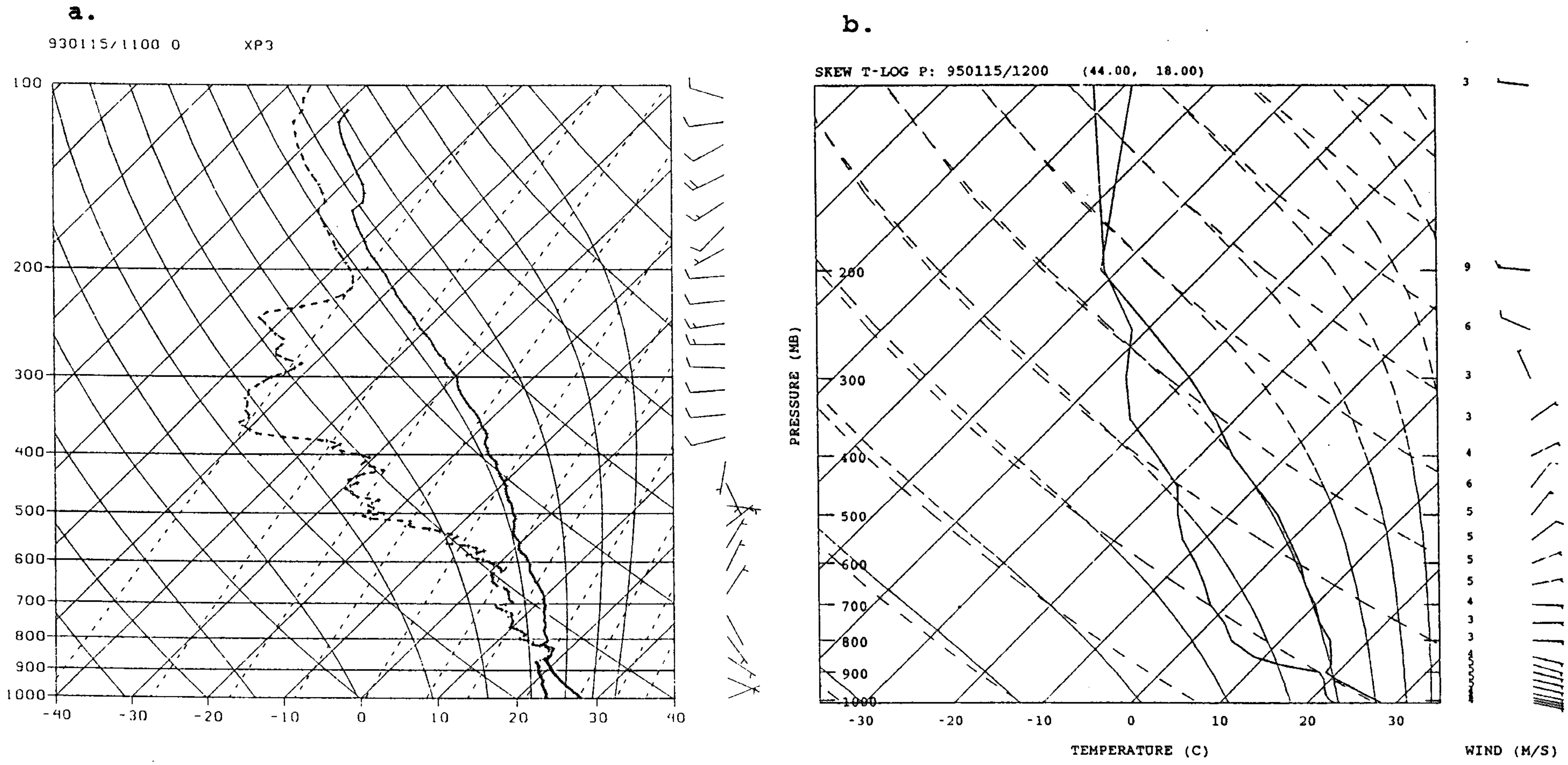

Figure 37. (a) R/V Shiyan 3 environmental sounding of 11 UTC 15 January 1993, (b) 36-h model forecast sounding of 12 UTC 15 January 1993.

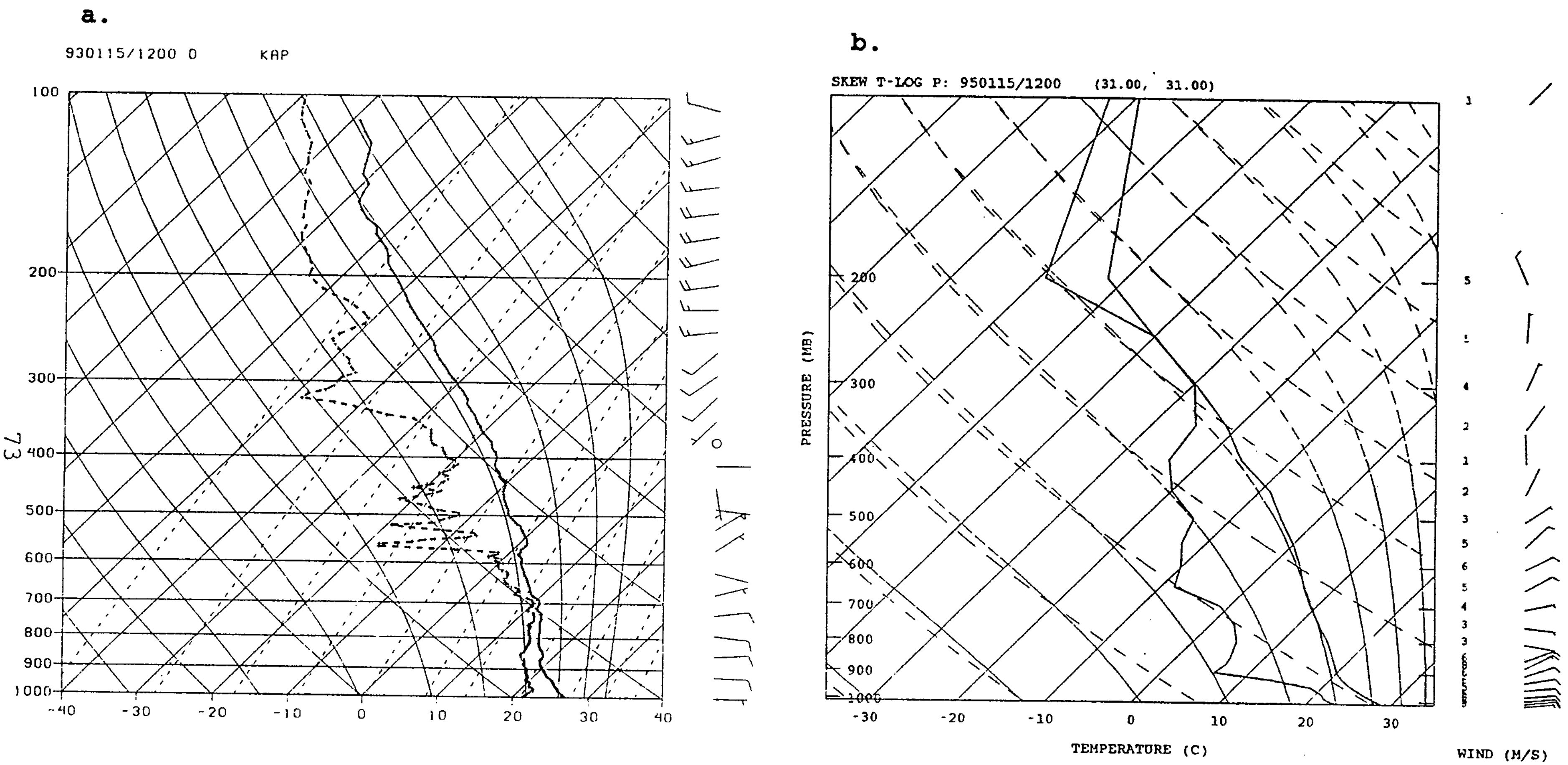

Figure 38. (a) Kapingamaranji environmental sounding of 12 UTC 15 January 1993, (b) 36-h model forecast sounding of 12 UTC 15 January 1993.

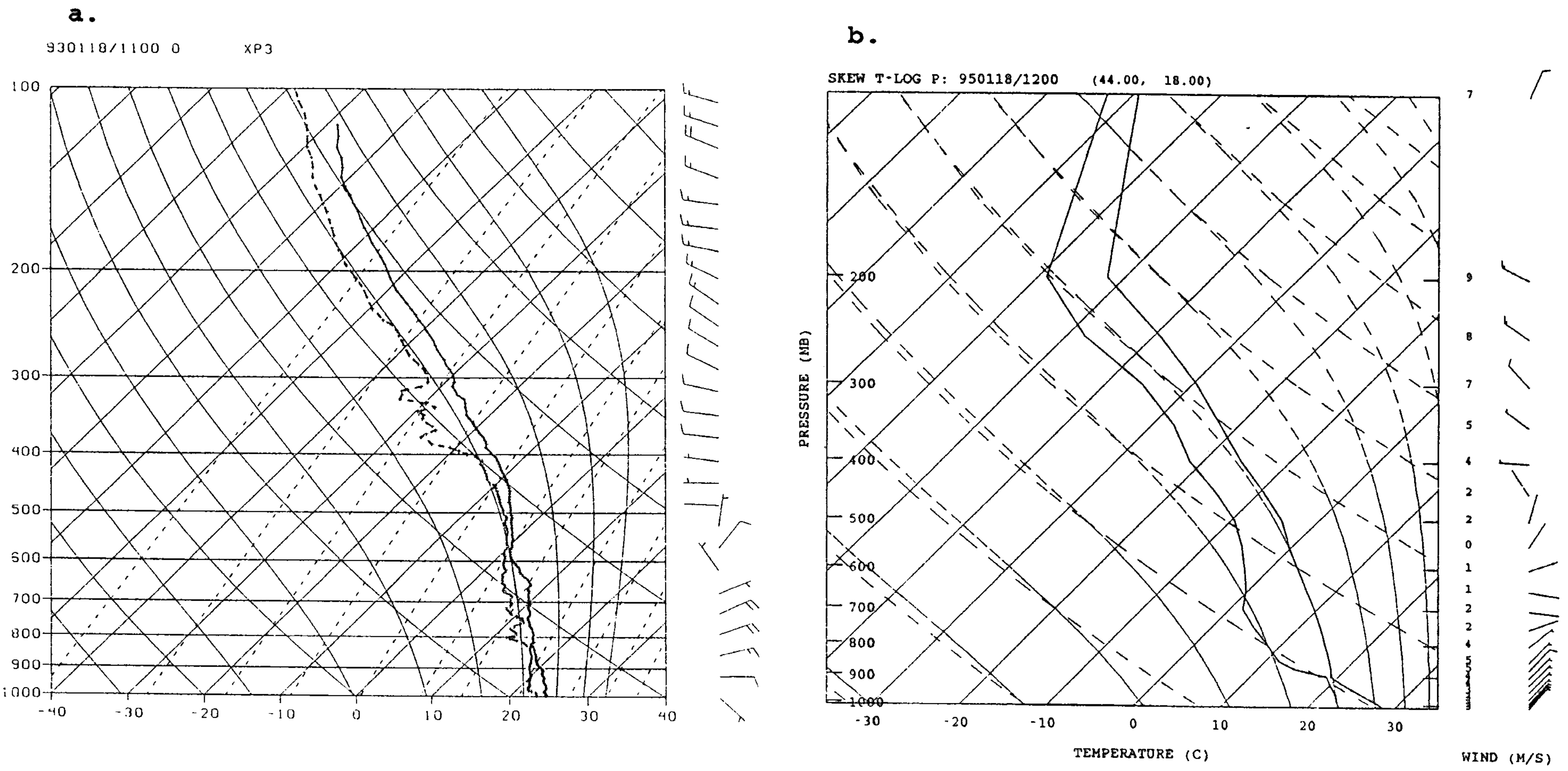

Figure 39. (a) R/V Shiyan 3 environmental sounding of 11 UTC 18 January 1993, (b) 12-h model forecast sounding of 12 UTC 18 January 1993.

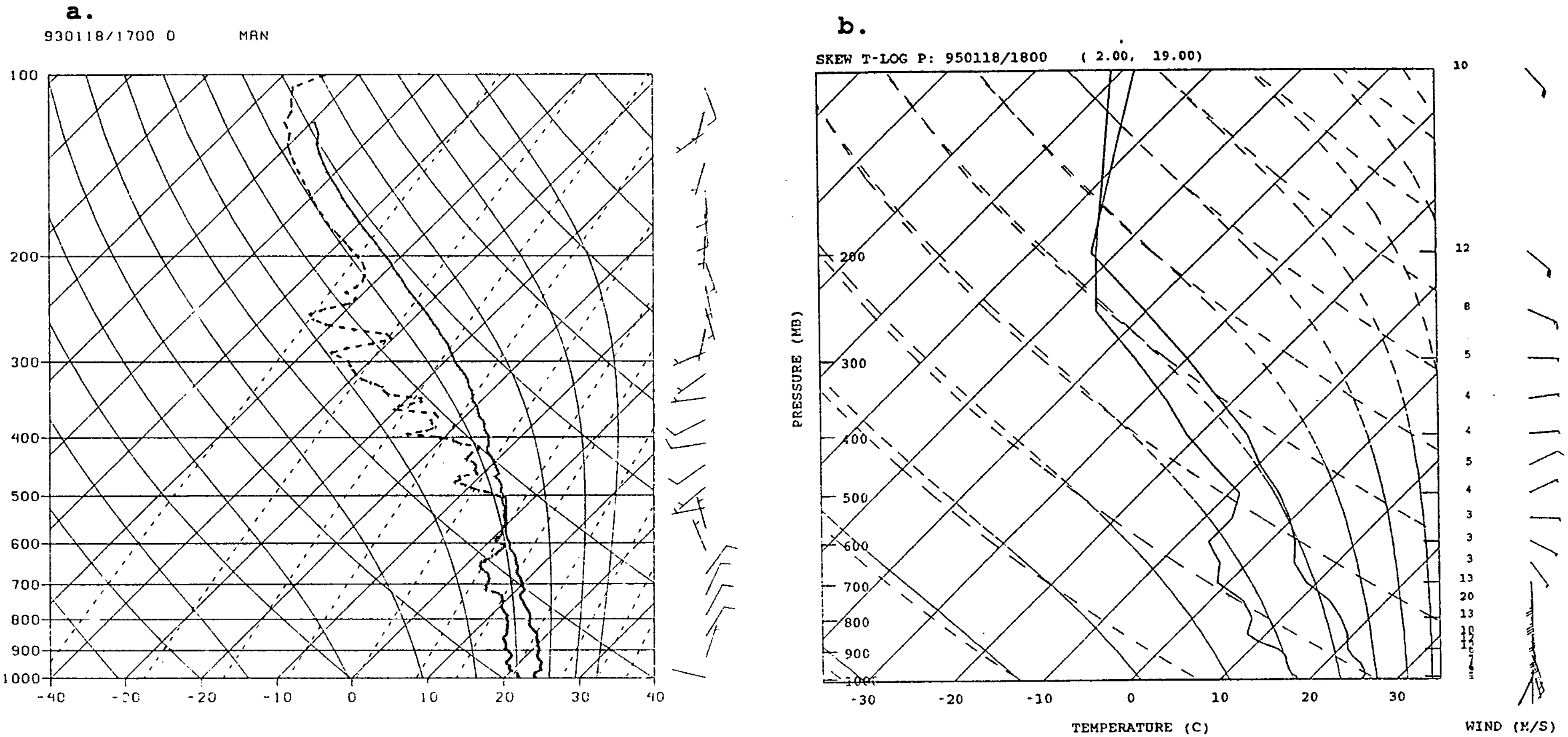

Figure 40. (a) Manus environmental sounding of 17 UTC 18 January 1993, (b) 18-h model forecast sounding of 18 UTC 18 January 1993.

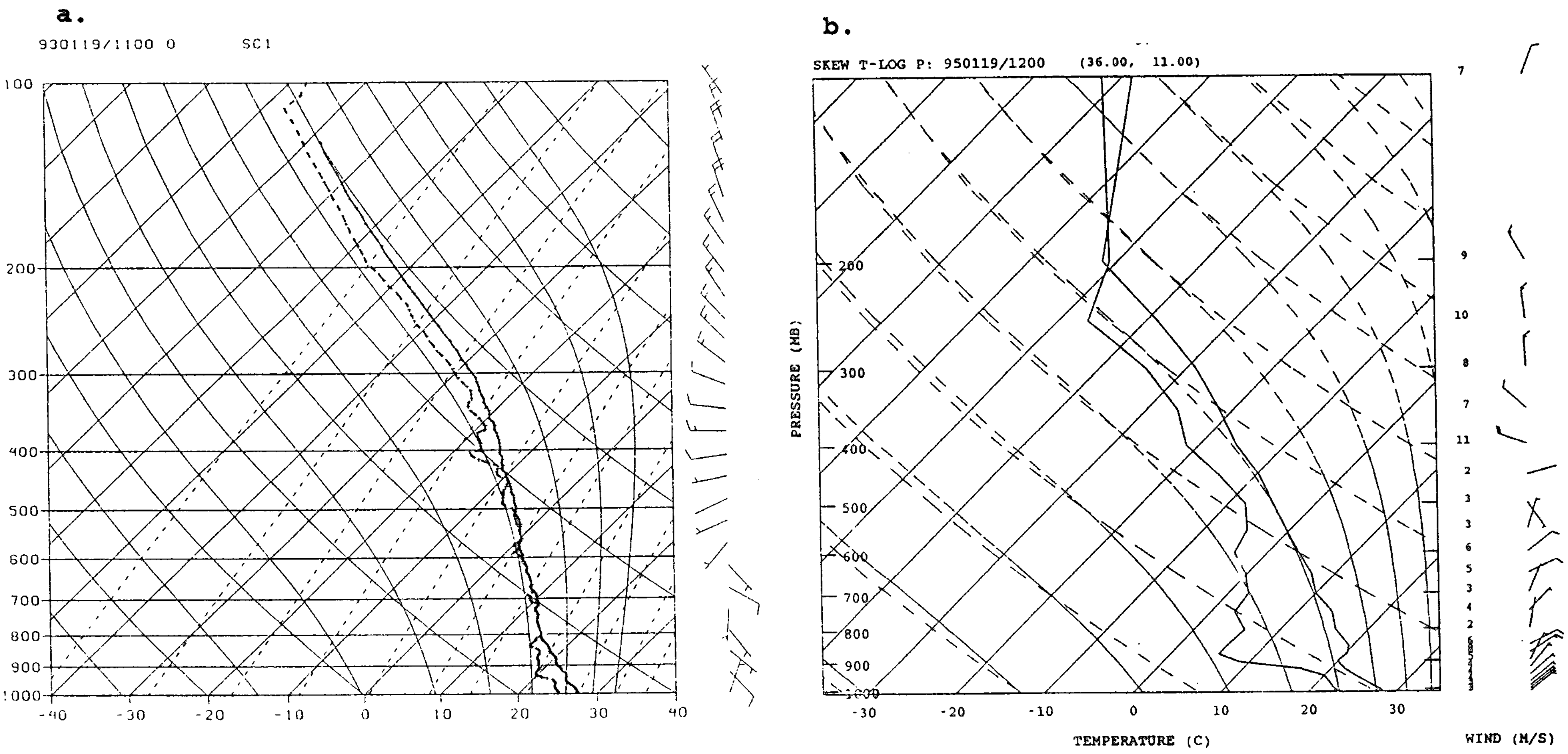

Figure 41. (a) R/V Kexue 1 environmental sounding of 11 UTC 19 January 1993, (b) 36-h model forecast sounding of 12 UTC 19 January 1993.

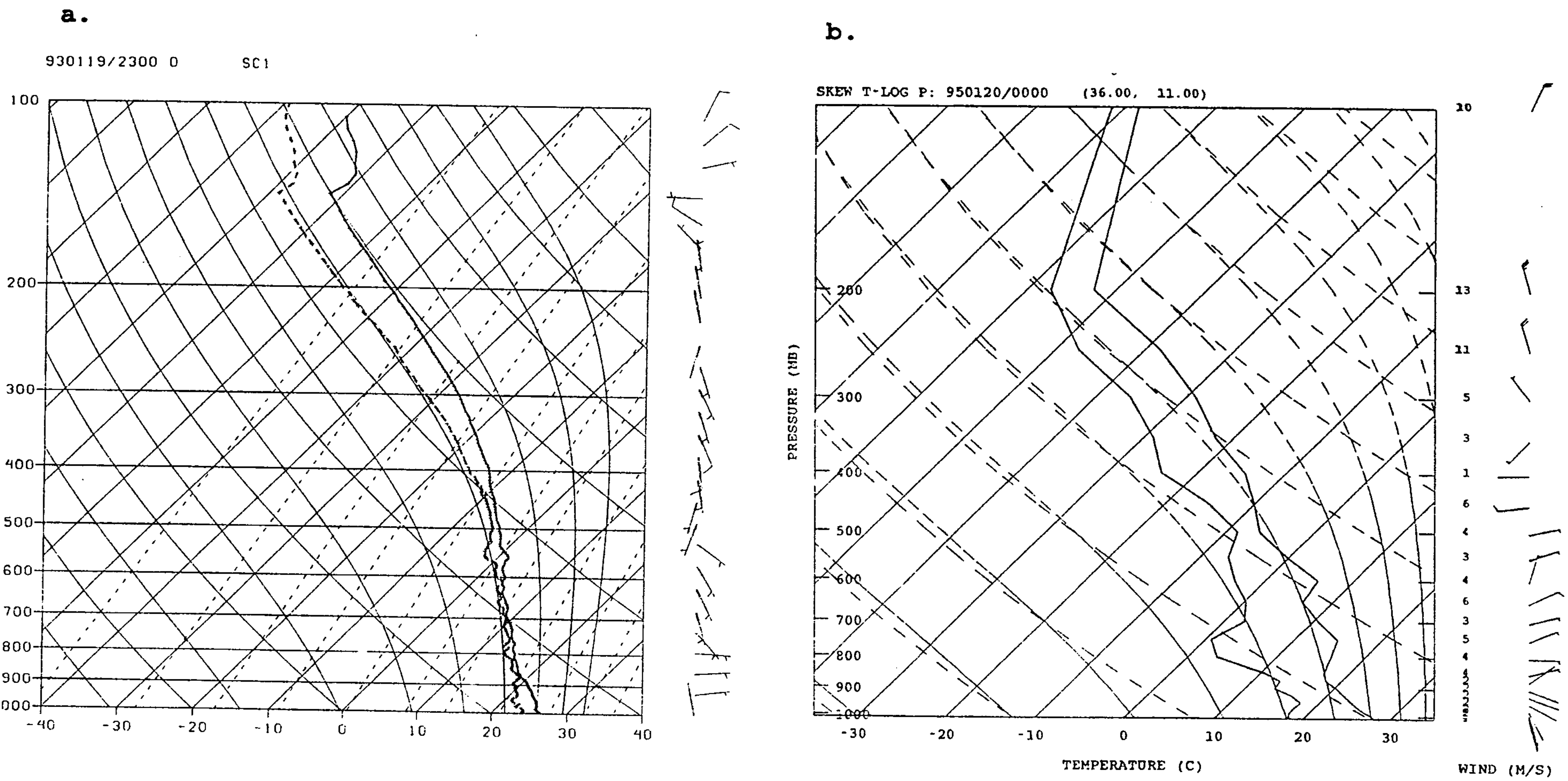

Figure 42. (a) R/V Kexue 1 environmental sounding of 23 UTC 19 January 1993, (b) 48-h model forecast sounding of 00 UTC 20 January 1993.

LIST OF REFERENCES

Albright, M.D., E.E. Recker, R.J. Reed, and R. Dang, 1985: The diurnal variation of deep convection in the central tropical Pacific during January-February 1979. *Mon. Wea. Rev.*, **113**, 1663-1680.

Blackadar, A.K., 1976: Modeling the nocturnal boundary layer. *Preprints Third Symposium Atmospheric Turbulence*, Diffusion and Air Quality, Raleigh, NC, Amer. Meteor. Soc., 46-49.

Brown, J., and K. Campana, 1978: An economical time-differencing system for numerical weather prediction. *Mon. Wea. Rev.*, **106**, 1125-1136.

Chang, S.W., 1979: An efficient parameterization of convective and non-convective planetary boundary layers for use in numerical models. *J. Appl. Meteor.*, **18**, 1205-1215.

Chang, S.W., R.J. Alliss, S. Raman, and J.J. Shi, 1993: SSM/I Observations of ERICA IOP 4 marine cyclone: A comparison with in situ observations and model simulation. *Mon. Wea. Rev.*, **121**, 2452-2464.

Charlock, T.P., and V. Ramanathan, 1985: The albedo field and cloud radiative forcing produced by a General Circulation Model with internally generated cloud optics. *J. Atmos. Sci.*, **42**, 1408-1429.

Chen, S.S., R.A. Houze, Jr., and B.E. Mapes, 1994: Satellite-observed cloud clusters during TOGA-COARE. *7th Conf. Satellite Met. and Ocean.*, Monterey, CA, Amer. Meteor. Soc., 22-25.

Chou, M.D., and L. Peng, 1983: A parameterization of the absorption in the 15 μm CO_2 spectral region with application to climate sensitivity studies. *J. Atmos. Sci.*, **40**, 2183-2192.

Ferandez, D., 1993: Incorporation and comparative evaluation of a non-convective cloud parameterization scheme in the Naval Research Laboratory West Coast Mesoscale Weather Prediction Model. M.S. Thesis, Naval Postgraduate School, Monterey, CA, 93943-5000, 77 pp.

Flament, P., and R. Bernstein, 1993: Images from the GMS-4 satellite during TOGA-COARE. Technical Report No. 93-12, University of Hawaii School of Ocean and Earth Science and Technology, 20 pp.

Gray, W.M., and R.W. Jacobson, 1977: Diurnal variation of deep cumulus convection. *Mon. Wea. Rev.*, **105**, 1171-1188.

Harshvardhan, R. Davies, D.A. Randall, and T.G. Corsetti, 1987: A fast radiation parameterization for atmospheric circulation models. *J. Geophys. Res.*, **92**, 1009-1016.

Holt, T., S. Chang, and S. Raman, 1990: A numerical study of the coastal cyclogenesis in GALE IOP 2: Sensitivity to PBL parameterizations. *Mon. Wea. Rev.*, **118**, 234-257.

Kuo, H.L., 1965: On formation and intensification of tropical cyclones through latent heat release by cumulus convection. *J. Atmos. Sci.*, **22**, 40-63.

Kuo, H.L., 1974: Further studies of the parameterization of the influence of cumulus convection of large scale flow. *J. Atmos. Sci.*, **31**, 1232-1240.

Lacis, A.A., and J.E. Hansen, 1974: A parameterization for the absorption of solar radiation in the earth's atmosphere. *J. Atmos. Sci.*, **31**, 118-133.

Madala, R.V., 1978: Efficient time integration schemes for atmosphere and ocean models. *Finite Difference Techniques for Vectorized Fluid Dynamic Calculations*, Springer-Verlag, 56-74.

Madala, R.V., S.W. Chang, U.C. Mohanty, S.C. Madan, R.K. Paliwal, V.B. Sarin, T. Holt, and S. Raman, 1987: Description of Naval Research Laboratory limited area dynamical weather prediction model. NRL Technical Report 5992, Washington, DC, 131 pp.

Mapes, B.E., and R.A. Houze Jr., 1993: Cloud clusters and superclusters over the oceanic warm pool. *Mon. Wea. Rev.*, **121**, 1398-1415.

Monin, A.S., and A.M. Yaglom, 1971: Statistical Fluid Mechanics, *Vol. 1*, MIT Press, Cambridge, MA.

Rodgers, C.D., 1968: Some extension and applications of the new random model for molecular band transmission. *Quart. J. Royal Meteor. Soc.*, **94**, 99-102.

Schrage, J., and D.G. Vincent, 1993: Climatology of the TOGA-COARE and adjacent regions 1985-1990. Vol. 1: Kinematic variables. [Available from Purdue University].

Slingo, J.M., and B. Ritter, 1985: Cloud prediction in the ECMWF model. ECMWF Technical Report No. 46, 48 pp. [Available from the European Centre for Medium Range Weather Forecasts, Shinfield Park, Reading RG2 9AX, UK].

Smolarkiewicz, P.K., 1983: A simple positive definite advection scheme with small implicit diffusion. *Mon. Wea. Rev.*, **111**, 479-486.

Stephens, G.L., 1984: The parameterization of radiation for numerical weather prediction and climate models. *Mon. Wea. Rev.*, **112**, 826-867.

Sundqvist, H., 1988: Parameterization of condensation and associated clouds in models for weather prediction and general circulation simulation. *Physically-Based Modelling and Simulation of Climate and Climatic Change*, M.E. Schlesinger, Ed., Reidel, 433-461.

Sundqvist, H., E. Berge, and J.E. Kristjansson, 1989: Condensation and cloud parameterization studies with a mesoscale numerical weather prediciton model. *Mon. Wea. Rev.*, **117**, 1641-1657.

Webster, P.J., and R.A. Houze Jr., 1991: The Equatorial Mesoscale Experiment (EMEX): An overview. *Bull. Amer. Meteor. Soc.*, **72**, 1481-1505.

Webster, P.J., and R. Lukas, 1992: TOGA-COARE: The coupled ocean-atmosphere response experiment. *Bull. Amer. Meteor. Soc.*, **73**, 1377-1416.

Wielicki, B.A., and R.M. Welch, 1986: Cumulus cloud properties derived using LANDSAT satellite data. *J. Climate Appl. Meteor.*, **25**, 261-305.

Williams, M., and R.A. Houze Jr., 1987: Satellite-observed characteristics of winter monsoon cloud clusters. *Mon. Wea. Rev.*, **115**, 505-519.

World Climate Research Programme (WCRP), 1985: Scientific plan for the Tropical Ocean Global Atmosphere Programme. WCRP publication #3, World Meteorological Organization, Geneva, 146 pp.

Zhao, Q., F. Carr, and G. Lesins, 1991: Improvement of precipitation forecasts by including cloud water and cloud ice into NMC's eta model. Preprints, *Ninth Conference on Numerical Weather Prediction*, 14-18 October, Denver, CO, 50-53.

INITIAL DISTRIBUTION LIST

		No. Copies
1.	Defense Technical Information Center Cameron Station Alexandria, Virginia 22304-6145	2
2.	Library, Code 52 Naval Postrgaduate School Monterey, California 93943-5101	2
3.	Chairman (Code MR/Hy) Department of Meteorology Naval Postgraduate School Monterey, California 93943-5000	1
4.	Chairman (Code OC/Bf) Department of Oceanography Naval Postgraduate School Monterey, California 93943-5000	1
5.	Dr. Teddy R. Holt Naval Research Laboratory-Monterey Monterey, California 93943-5006	2
6.	Professor Russell L. Elsberry (Code MR/Es) Department of Meteorology Naval Postgraduate School Monterey, California 93943-5000	1
7.	Commander Naval Meteorology and Oceanography Command Stennis Space Center, MS 39529-5000	1
8.	Commanding Officer Fleet Numerical Meteorology and Oceanography Center Monterey, California 93943	1
9.	LT Patrick L. Waring Naval European Meteorology and Oceanography Detachment PSC 812 Box 3380 FPO AE 09627-3380	1